The Astrophysical Journal, 892:69 (25pp), 2020 March 20 https://doi.org/10.3847/1538-4357/ab7760

A Two Carrier Families Spectral Profile Model for Anomalous Microwave Emission

L. S. Bernstein[1,2], R. M. Shroll[1], J. Quenneville[1], and C. Dickinson[3]
[1] Spectral Sciences, Inc., 4 Fourth Ave., Burlington, MA 01803, USA; larry@spectral.com, rshroll@spectral.com, jasonq@spectral.com
[2] Maine Molecular Sciences, Suite 305B-1, 14 Maine St., Brunswick, ME 04011, USA; spectral1949@gmail.com
[3] Jodrell Bank Centre for Astrophysics, Alan Turing Building, School of Physics and Astronomy, The University of Manchester, Oxford Road, Manchester, M13 9PL, UK; clive.dickinson@manchester.ac.uk
Received 2018 November 6; revised 2020 February 14; accepted 2020 February 14; published 2020 March 30

Abstract

We model anomalous microwave emission (AME) spectral profiles from 14 diverse galactic and extragalactic sources. The spectral profile model is an analytic representation of a quantum mechanical model for symmetric top rotational emission. The observed spectral shapes are well fit by superposing two model profiles originating from two distinct carrier families. Each family is composed of numerous, comparably abundant isomers of a parent carrier. The isomers have similar rotational constants, thereby producing continuous, versus resolved line, spectra that are slightly broader than the parent profiles. Ten observations are fit with comparable peak height and peak frequency ratios for the two carrier families, suggesting that AME arises from common carriers. One observation is fit using a single family, attributed to photodissociation of the less stable, smaller molecules for the missing family. Three observations are fit by combining two frequency-shifted model spectra, indicating multiple sources along their sight lines. The derived rotational constants for the two parent carriers are well determined because their rotational temperature is well characterized for the LDN 1622 dark cloud AME source. The rotational constants are consistent with the C_{36} and C_{60} fullerenes as the parent carriers. We use a Monte Carlo simulation of fullerene hydrogenation to understand the origins of source variability in the AME model fits. Other potential carriers, polycyclic aromatic hydrocarbons and very small grains, cannot be excluded; however, we find that fulleranes are also viable carriers because their aromatic cages are extremely stable to photodissociation, and their data-derived sizes suggest C_{36} and C_{60} parent fullerenes.

Unified Astronomy Thesaurus concepts: Radio sources (1358); Radio spectroscopy (1359); Molecular spectroscopy (2095); Theoretical models (2107); Astronomy data modeling (1859)

1. Introduction

Anomalous microwave emission (AME) is a foreground emission feature, typically peaking near 25 GHz, which overlays the cosmic microwave background (CMB). AME is widespread and variable, emanating from diverse galactic and extragalactic sources. The discovery of AME, some two decades ago (Kogut et al. 1996; Leitch et al. 1997), has opened a new observational window for the exploration and characterization of dust grains and molecules in the interstellar medium (ISM). For a recent in-depth review of "The State-of-Play of AME Research," see Dickinson et al. (2018).

Understanding the origin of AME has far-reaching implications with regard to the chemical composition and abundances of large molecules, more than ∼20 C atoms, and very small grains, radii of ∼4–20 Å, in the ISM. On the other hand, researchers investigating the spatial variability of the CMB regard AME as a contaminating spectral feature. Addressing both perspectives, understanding AME and separating it from the CMB requires accurate models for AME, as well as for the other overlapping foreground contributions from free–free, synchrotron, and dust thermal emissions (Bonaldi et al. 2007; Leach et al. 2008).

The identities of the AME carriers remain elusive. It is widely held that AME is due to electric dipole emission from an assortment of rotating molecules and/or very small spinning dust grains (VSGs; Draine & Lazarian 1998a, 1998b). There is a chemically diverse inventory of candidate carriers, including polycyclic aromatic hydrocarbons (PAHs; Draine & Lazarian 1998b), large fulleranes (hydrogenated fullerenes with 60 or more carbon atoms; Iglesias-Groth 2005, 2006), carbonaceous and noncarbonaceous grains (Hensley & Draine 2017), and, most recently, nanodiamonds (Greaves et al. 2018).

Several studies have called into question the viability of PAH molecules as the AME carriers (Battistelli et al. 2015; Tibbs et al. 2015b; Hensley et al. 2016). This is a puzzling finding, in that PAH molecules are widely believed to be in abundance as the carriers of the ubiquitous interstellar mid-infrared emission bands (Tielens 2008; Peeters 2011). If PAH molecules are plentiful, then they are expected be a significant contributor to AME.

The physics-based AME spectral models (Draine & Lazarian 1998a, 1998b; Ali-Haïmoud et al. 2009; Hoang et al. 2010, 2016; Ysard & Verstraete 2010; Silsbee et al. 2011) provide good fits to the diversity of AME spectra from many different sources (see references and examples in Planck Collaboration 2011b; Dickinson et al. 2018). A rigorous treatment of the physics of spinning dust emission in different interstellar environments results in some 14 fitting parameters, consisting of 7 for the environment, 1 for column density, and 6 for the dipole moment and size distributions (Draine & Lazarian 1998a, 1998b). Some of the parameters are degenerate with respect to their effects on the intensity and shape of an AME spectrum. The information content of a single AME spectrum is low, because (1) it is usually composed of a small number, typically 20 or fewer, of noisy spectral points and (2) it has a simple shape, primarily characterized by two parameters, its peak emission frequency, and width. As a consequence of fitting parameter uncertainties, parameter degeneracies, and low spectral information content, it has been

challenging to definitively specify the type, molecule or grain, sizes, and abundances of the AME carriers.

In this study, we seek the identities of the AME carriers by considering the commonality among many varied AME sources and spectra. We model the AME spectra from 14 diverse sources in order to better constrain the type (e.g., PAH, fullerane, VSG, etc.) and the sizes of the AME carriers. The spectral model employed is an analytic representation of the quantum mechanical rotational emission model for symmetric top carriers used by Ysard & Verstraete (2010) in their analysis of AME spectra.

We explore a new paradigm for the AME carriers, where the observed spectra are fit with a superposition of two model profiles, with each profile originating from a distinct carrier family. We refer to this approach as the two carrier families (2CF) spectral model. Each family is presumed to be composed of numerous, comparably abundant isomers of a parent carrier. The isomers have similar rotational constants, thereby producing a continuous, versus line, spectrum that is slightly broader than the parent profile. The 2CF model is not specific to a carrier type; however, in this study, as discussed below, we choose to focus on fullerane carriers.

Spectral shape, augmented by additional information, can provide a good estimate of the size of a carrier, such as the number of carbon atoms, N_C, for a carbonaceous carrier. Estimation of carrier size, which, for the case of spherical carriers, is encoded in a single rotational constant, B, entails resolving the so-called BT_{rot} ambiguity (Bernstein et al. 2015). The ambiguity arises because the shape of a rotational spectrum depends only on the product of the rotational constant and the effective rotational temperature, T_{rot}. Hence, in order to untangle BT_{rot} and retrieve the carrier size, one needs an independent measure of T_{rot}.

Determining T_{rot} for an AME source is challenging. We use T_{rot} to approximately describe rotational state populations, even though the entire system is not necessarily at equilibrium. Rotational energy transfer via collisions is efficient, and an effective T_{rot} is often meaningful, even if other degrees of freedom, such as vibration, are out of equilibrium. T_{rot} depends on a variety of excitation and relaxation mechanisms whose quantitative evaluation depends on knowledge of multiple sight-line-specific physical properties and also on intrinsic carrier properties (Draine & Lazarian 1998a). The physical properties include the interstellar radiation field, in both the ultraviolet (UV) and microwave; the gas kinetic temperature; and the number densities of the most abundant species, H, H_2, He, and H^+. The intrinsic carrier properties include the UV and microwave absorption cross sections, the collisional excitation and relaxation cross sections with all the major ambient species, whether or not the carrier is ionized, the extent of hydrogenation, and the magnitude of its dipole moment. Fortunately, there is a type of AME source, namely, a dark cloud (DC), that circumvents the need to quantify most of the above physical and carrier intrinsic quantities in order to establish a good estimate of T_{rot}. As discussed later, the relatively high density in a DC implies that $T_{rot} = T_K$, where T_K is the gas kinetic temperature. This study includes the LDN 1622 DC for which T_K has been narrowly constrained, thereby allowing us to establish well-determined values for the parent carrier sizes.

For several reasons, we explore the viability of fullerenes as the parent carriers, noting that AME arises from the dipolar fullerane family members. First, fullerenes, by virtue of their resilient cage structure, are extremely stable with respect to UV photodissociation in the ISM (Kroto 1988; Berné et al. 2015; Omont 2016). Second, the only large molecules that have been identified in the ISM are fullerenes. C_{60}^+ has been identified as the carrier of several near-infrared diffuse interstellar bands (DIBs; Ehrenfreund & Foing 2010; Campbell et al. 2015; Walker et al. 2015), and C_{60} and C_{70} bands have been observed in some of the unidentified infrared (UIR) emission spectra (Cami et al. 2010, 2011; García-Hernández et al. 2010; Sellgren et al. 2010; Roberts et al. 2012; Berné et al. 2013, 2017; Castellanos et al. 2014). It is natural to conjecture that the less well understood smaller fullerenes might also be present in significant abundance in the ISM. Kroto (1987) suggested that the small fullerenes, C_{20}, C_{24}, C_{28}, C_{32}, and C_{36}, may have "enhanced stability relative to near neighbors" (e.g., C_{22} is a neighbor to C_{20} and C_{24}). Third, small fullerenes and fulleranes have been shown to be plausible carriers for some prominent UIR and DIB bands. Bernstein et al. (2017) demonstrated that the spectral profiles of the 11.2 and 12.7 μm UIR bands could be well fit based on C_{24} spectroscopy. In more recent work, Bernstein et al. (2018) found that a small fullerane and PAH, with 30 or fewer C atoms, were plausible common carriers for the 6614 and 6196 Å DIBs.

This paper is organized as follows. The subsequent section overviews the observed AME spectra for a wide variety of galactic and extragalactic sources. This is followed by a description of our AME spectral model and its application to fitting the observed AME spectra. Then, we address resolution of the BT_{rot} ambiguity and present estimates of carrier sizes. Next, the broader implications of small fullerenes and fulleranes as potentially abundant interstellar molecules are discussed. Then, recommendations for future investigations are presented. Finally, we summarize the key findings. Further details of the underlying theory are described in appendices, including (1) derivation of the analytic AME spectral model (Appendix A), (2) spectral fitting methodology (Appendix B), (3) angular momentum distributions (Appendix C), (4) dipole moments and rotational constants of fullerene analogues (Appendix D), (5) carrier abundance estimation (Appendix E), and (6) accretion of fullerenes onto grains (Appendix F).

2. AME Data and Sources

We model the residual AME spectra obtained after subtracting the overlapping spectral contributions of free–free, dust thermal, and synchrotron emissions from the observed spectra. The residual AME spectra investigated here are presented in Figures 1–3, along with their spectral fits, which are discussed in a later section. Figure 1 features single-source AME spectra, Figure 2 features very sparsely sampled spectra, and Figure 3 features multiple-source spectra. The noise level for all residual AME spectra increases rapidly beyond ~60 GHz owing to the difficulty in accurately subtracting the increasing and dominant contribution from the red tail of the dust thermal emission. The data values and error bars were obtained from tabulated data or digitized from published AME spectra in the references cited in the following source summary Sections 2.1–2.13. The small additional error, ~±1%, due to digitization is inconsequential with respect to the results of this study.

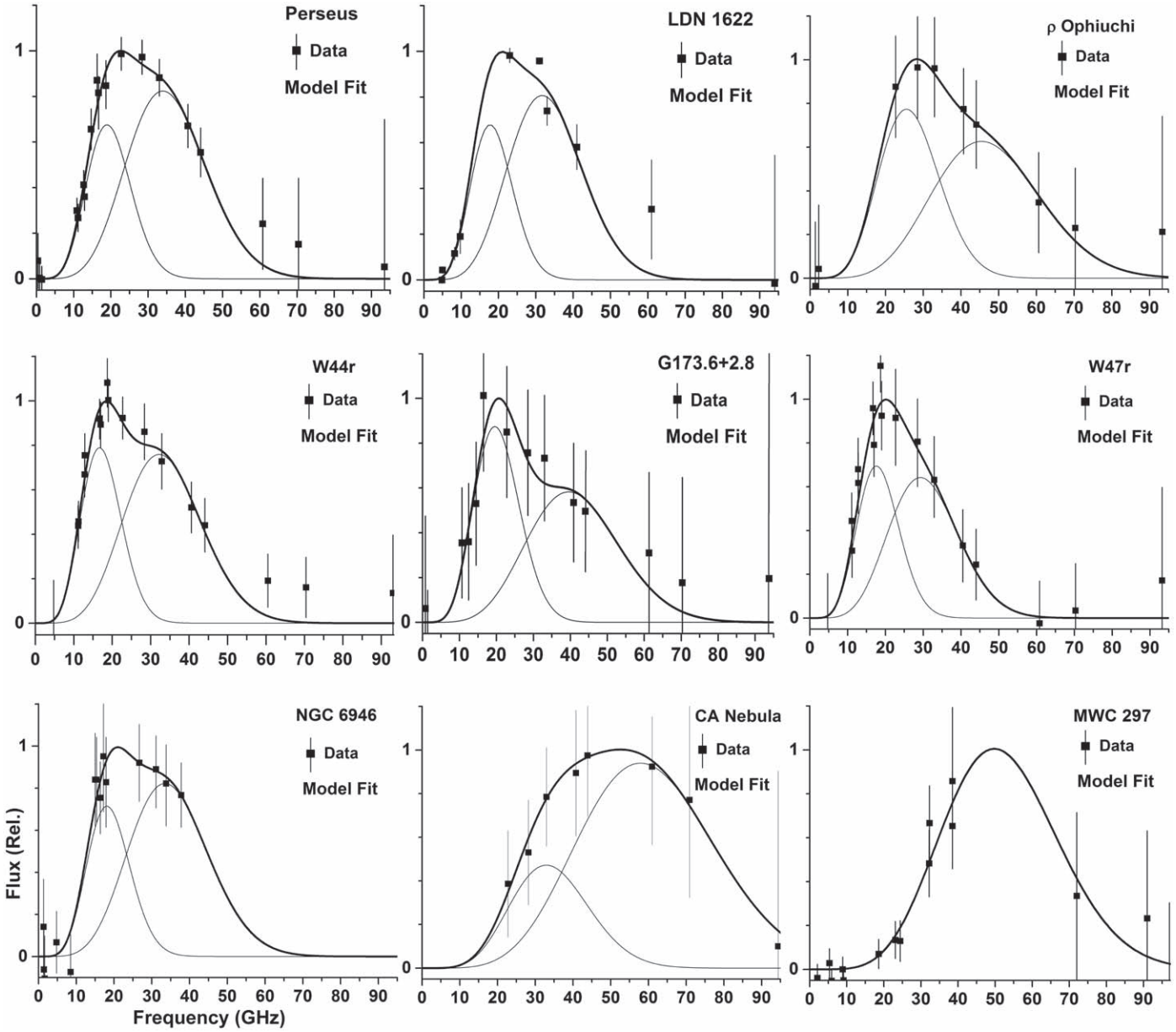

Figure 1. Comparison of the observed AME spectra (black squares with vertical lines for uncertainties) to the 2CF spectral model fits (thick black lines). The two carrier components contributing to each fit are shown by the thin black lines. We note that the MWC 297 fit (bottom right panel) required only a single carrier component. The 2CF model and the data fits are discussed in Section 3 and Appendix B.

Ignoring, for now, the spectral fits to the data, it is difficult to discern any commonality among the observed spectra, particularly with respect to their shapes. The apparent lack of commonality arises from a combination of sparse spectral sampling and spectral shifting on the peak locations. The model fits, discussed later, provide a good approximation to the full spectral shape and make the similarities and differences among the spectra more apparent.

2.1. Perseus G159.6−18.5

The Perseus G159.6−18.5 AME spectrum is the quintessential AME spectrum because it features the best spectral coverage and spectral sampling combined with high signal-to-noise ratio (Watson et al. 2005; Planck Collaboration 2011b; Génova-Santos et al. 2015; Dickinson et al. 2018). The data and uncertainties originate from Figure 7 in Génova-Santos et al. (2015). Perseus is categorized as a molecular cloud (MC; Draine & Lazarian 1998b). Its physical properties are well characterized. Based on analysis of C_2 optical emission spectra, Iglesias-Groth (2011) retrieved the gas kinetic temperature, $T_K = 40$ K, and density, $n_{H_2} = 250\,\mathrm{cm}^{-3}$, for a sight line nearly coincident with that for the AME observations.

2.2. Lynds Dark Nebula (LDN) 1622

The shape of the LDN 1622 AME spectrum (Finkbeiner et al. 2002; Finkbeiner 2004; Casassus et al. 2006) is nearly identical to that for Perseus. The free–free and dust thermal emission subtracted data and uncertainties originate from Figure 10 in Casassus et al. (2006). LDN 1622 is considered a DC with physical properties of $T_K = 15$–22 K and $n_{\mathrm{H}} = 1 \times 10^4\,\mathrm{cm}^{-3}$ (Iglesias-Groth 2006; Harper et al. 2015).

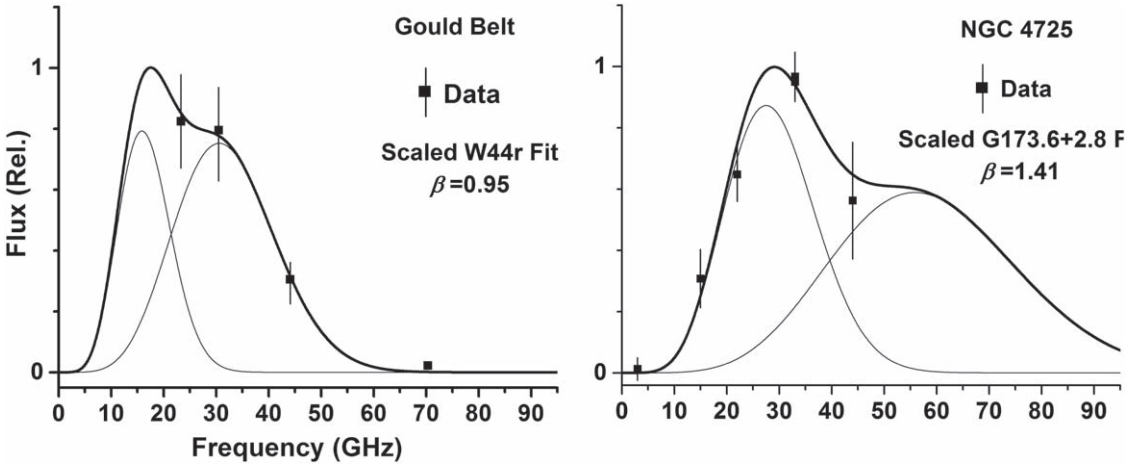

Figure 2. Comparisons of the observed, and very sparsely sampled, Gould Belt and NGC 4725 AME spectra to the closest-matching model spectrum from Figure 1 (thick black line). A frequency scale shift, $\nu' = \beta\nu$, was applied to the model spectra to move them onto the sparsely sampled spectra. The two carrier components contributing to each fit are shown by the thin black lines (see Section 3.4 for details).

2.3. ρ *Ophiuchi W*

The ρ Ophiuchi W AME spectrum (Casassus et al. 2008; Planck Collaboration 2011b) arises from a photodissociation region (PDR; Casassus et al. 2008). The data and uncertainties originate from Table 3 in Planck Collaboration (2011b). The ρ Ophiuchi spectrum is similar in shape to Perseus but peaks at a slightly higher frequency. This indicates a slightly higher $T_{\rm rot}$ for ρ Ophiuchi (i.e., $T_{\rm rot} \propto \nu_p^2$). The modeled physical properties of the ρ Ophiuchi AME source are $T_K = 20$ K and $n_{\rm H} = 2 \times 10^4\,{\rm cm}^{-3}$ (Planck Collaboration 2011b).

2.4. CA Nebula

The CA Nebula AME spectrum (Planck Collaboration 2011b, 2014) is unusual, as it peaks at a much higher frequency, ∼50 GHz, than the majority of other spectra, which peak in the vicinity of 25 GHz. The data and uncertainties originate from Figure 17 in Planck Collaboration (2014). The AME source is embedded in a bright H II region, as opposed to relatively dark regions for the other sources. However, it is not clear whether or not the CA Nebula AME source is characterized by the physical properties of an H II region. There is speculation that the source may be a PDR (Planck Collaboration 2014).

2.5. W44r

The W44r AME spectrum is associated with an environment characterized by the interaction of a supernova remnant (SNR) with several surrounding MCs (Irfan et al. 2015; Génova-Santos et al. 2016). The data and uncertainties originate from Figure 6 in Génova-Santos et al. (2016). The best single environment model fit to the W44r spectrum employs the warm neutral medium (WMN; Génova-Santos et al. 2016) with characteristic physical properties of $T_K = 6000$ K and $n_{\rm H} = 0.4\,{\rm cm}^{-3}$, with a 0.1 mole fraction of H^+. While the WNM environment provides a good fit to the W44r AME spectrum, it may not represent the actual physical conditions in W44r. Based on analyzing radio and gamma-ray emissions from W44, Cardillo et al. (2014) derived an average gas density, $n_{\rm H} \sim 300\,{\rm cm}^{-1}$, nearly two orders of magnitude higher than that for the WNM fit.

Other SNR AME observations of note include 3C 396 (AMI Consortium 2009) and IC 443 (Loru et al. 2018). The IC 443 spectrum has good spectral coverage over the AME spectral region, and its profile appears similar to that for W44r.

2.6. NGC 6946

The NGC 6946 AME spectrum represents the first extragalactic detection of AME (AMI Consortium et al. 2010; Murphy et al. 2010). The baseline subtraction, data, and uncertainties originate from Figure 3 (right panel) in AMI Consortium et al. (2010). The spinning dust model (Ali-Haïmoud et al. 2009) fit to the NGC 6946 spectrum is based on perturbing the WNM properties (Murphy et al. 2010), with dust model determined physical properties of $T_K = 10{,}000$ K and $n_{\rm H} = 1.0\,{\rm cm}^{-3}$, with a 0.01 mole fraction of H^+. The spectral coverage for NGC 6946 is limited, with just a few points in the peak and shoulder spectral regions; however, it appears to be consistent with most of the other example spectra in Figure 1 in these spectral regions.

2.7. Protoplanetary Disks

AME spectra were recently reported for three protoplanetary disk (PPD) sources, MWC 297, HD 97048, and V892 Tau, which also harbor nanodiamonds (Greaves et al. 2018). The MWC 297 data and uncertainties originate from Figure 3 in Greaves et al. (2018). Because the spectra are noisy and sparsely sampled, we focused on the best exemplar, MWC 297, for further consideration. The locations and physical properties of the regions within, or outside of, the PPD where the AME emanates from are not well characterized. The peak frequencies of the three AME spectra are significantly different: 18, 25, and 49 GHz for V892 Tau, HD 97048, and MWC 297, respectively. The three PPD spectra are quite narrow. Their widths are about half the width of other AME spectra with comparable peak frequencies.

2.8. W43r

The W43r AME spectrum (Irfan et al. 2015; Génova-Santos et al. 2016) is of interest because it is associated with an "extreme molecular cloud and star-forming region" (Luong et al. 2011). W43 is characterized as a complex structure of MCs, with ∼12% of its total mass residing in multiple clumps of dense protostellar material. The data and uncertainties

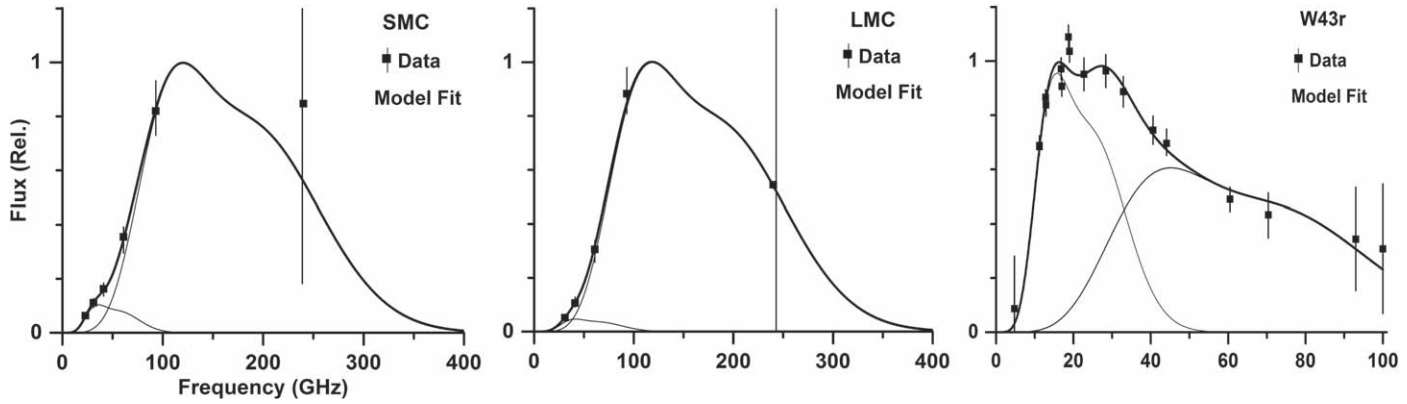

Figure 3. Comparisons of the observed SMC, LMC, and W43r AME spectra (black squares with vertical lines for the uncertainties) to model fits (thick black line) based on superposing two, shifted ⟨AME⟩ reference spectra as defined in Table 1 (thin black lines). These spectra are distinguished from those in Figure 1, in that they appear to possess two distinct sources along their sight lines. Details of the model and the data fits are presented in Section 3.5.

originate from Figure 6 in Génova-Santos et al. (2016). The physical properties of the W43r AME source are not known. As noted by Génova-Santos et al. (2016), the W43r AME spectrum cannot be simply fit in terms of the standard spinning dust environment modes. However, there are constraints on its temperature. Spatially resolved CO rotational temperature measurements established an average temperature for W43 of $T_{\rm rot} = 10$ K and a temperature range of $T_{\rm rot} = 5$–18 K (Luong et al. 2011). The W43r AME spectrum is also interesting because of its unusually large width compared to the other example spectra in Figure 1.

W43r is a low Galactic latitude source (within 1° of the Galactic plane) where line-of-sight integration may include multiple components, thus broadening it in general. There are multiple sources within the W43 complex. For example, Rathborne et al. (2009) detect over 20 distinct sources with CO emission lines, although most of them are at a similar velocity. Without higher-resolution radio data it is not possible to know which of these are emitting, or whether it is all of them equally, or even if the emission is coming from in between the clouds (unlikely, but possible).

2.9. W47r

Little is known about W47r. We include it here because its AME spectrum has good spectral coverage (Irfan et al. 2015; Génova-Santos et al. 2016). The data and uncertainties originate from Figure 6 in Génova-Santos et al. (2016). W47r is characterized by a wide variety of environments, including H II regions, molecular complexes, and several weak SNRs (Irfan et al. 2015; Génova-Santos et al. 2016).

2.10. G173.6+2.8

G173.6+2.8 is of astrophysical interest because it is embedded in a massive star-forming region located toward the galactic anticenter (Planck Collaboration 2011b). The data and uncertainties originate from Figure 12 in Planck Collaboration (2011b). It also has good spectral coverage of its AME spectrum. The best spinning dust model fit to the G173.6+2.8 AME spectrum is based on the cold neutral medium (CNM) environment parameters with $T_K = 100$ K and $n_{\rm H} = 30\,{\rm cm}^{-3}$ (Draine & Lazarian 1998a; Planck Collaboration 2011b).

2.11. Large and Small Magellanic Clouds

The Large and Small Magellanic Clouds (LMC and SMC) exhibit AME-like excess emission at much higher frequencies than is typical for AME (Bot et al. 2010; Israel et al. 2010). The data and uncertainties originate from Figure 6 in Bot et al. (2010) and correspond to the "millimeter excess" after subtraction of the free–free, dust thermal emission, and synchrotron contributions. The SMC and LMC spectra are sparsely sampled, peaking within the ∼100–200 GHz spectral range, as compared to ∼25 GHz for most AME spectra. The LMC and SMC spectra are integrated over relatively large areas and likely represent an average over diverse sources. One would expect that source averaging would significantly broaden the spectra. However, this does not appear to be the case. Although the LMC and SMC spectra are fit well with a spinning dust model based on a combination of PPDs and diffuse ISM environments (Bot et al. 2010), spinning dust emission is considered a "promising" but not definitive explanation of the excess emission (Planck Collaboration 2011a; Draine & Hensley 2012).

2.12. Gould Belt

The Gould Belt AME spectrum (Planck Collaboration 2013) is of interest because it originates in a much lower density environment than the other spectra, the diffuse ISM, and it occurs on large angular scales (i.e., degrees). The data and uncertainties originate from Figure 10 in Planck Collaboration (2013). The physical conditions of the environments giving rise to the Gould Belt AME are not well constrained. Model fits using SPDUST (Ali-Haïmoud et al. 2009; Silsbee et al. 2011) suggest that the dominant environmental component is the CNM with typical physical properties of $T_K = 100$ K and $n_{\rm H} = 30\,{\rm cm}^{-3}$.

2.13. NGC 4725

The NGC 4725 AME spectrum originates from a recent extragalactic detection of AME (Murphy et al. 2018). The free–free subtraction, data, and uncertainties originate from Figure 4 in Murphy et al. (2018). Like the extragalactic AME source, NGC 6946, the model fit for NGC 4725 is also based on WNM properties, with model estimated parameters of $T_K = 10{,}000$ K and $n_{\rm H} = 1.25\,{\rm cm}^{-3}$, with a 0.1 mole fraction of H^+ (Murphy et al. 2018). While the observed NGC 4725 spectrum consists of a limited number of frequencies, they are well situated and provide good definition of the steep red edge and peak spectral regions.

3. AME Spectral Model and Data Fits

3.1. Analytic AME Spectral Model

We describe an AME spectral model for a single molecular or small grain carrier. This model was used to fit the observed AME spectra as a weighted sum of modeled profiles for the individual carriers. The spectral fitting was performed with an analytical representation of the quantum mechanical (QM) model used by Ysard & Verstraete (2010) for symmetric top AME carriers (see Appendix A for details of the QM model).

We assume that the carriers are most likely symmetric tops. Linear molecules are less likely to be the carriers because they cannot persist in the intense UV radiation fields associated with some of the AME sources (i.e., it is easier to break a chain by cleaving a single bond). Furthermore, the spectral profile of a slightly asymmetric top can be reasonably modeled in terms of an effective symmetric top geometry.

The analytic model for the rotational emission profile of a symmetric top carrier is given by

$$S(\upsilon) = S_p a_n \left\{\frac{\upsilon}{\upsilon_p}\right\}^n \exp\left(-\frac{n}{2}\left\{\frac{\upsilon}{\upsilon_p}\right\}^2\right), \quad (1)$$

where S_p is the peak emission intensity at the frequency ν_p, a_n is a normalization constant such that $S = S_p$ at ν_p, and $n = 5$ or 6 for linear or symmetric top molecules, respectively (see Appendix A). The dependence of S_p on the physical properties of the carrier and its environment are specified in Appendix A. The normalization constant is defined by

$$a_n = \exp\left(\frac{n}{2}\right). \quad (2)$$

The frequency for the peak emission intensity is related to carrier-specific parameters (see Appendix A) through

$$\upsilon_p = \sqrt{\frac{2n}{c_2} B T_{\rm rot}}\,, \quad (3)$$

where the assumed units for evaluation of this expression are $B(\mathrm{cm}^{-1})$, ν_p (cm^{-1}), and $c_2 = 1.4388$ K cm.

Some example spectral profiles for the analytic model for different choices of the parameter n are displayed in Figure 4. For linear and symmetric top carriers $n = 5$ and 6, respectively. We see that the basic impact of varying n is on profile width. Thus, using a lower value of n than that corresponding to a given carrier geometry provides a convenient way to introduce variance into the profile. The physical origins of the variance are the distributions of rotational temperatures and carrier sizes for a particular AME source.

3.2. Perseus and the 2CF Spectral Model

The 2CF spectral model originated from an initial focus on modeling the Perseus spectrum. While the Perseus spectrum has the best spectral coverage of all the observed AME spectra, it is still a sparsely sampled and relatively noisy spectrum. The Perseus spectral profile exhibits a slightly asymmetric peak region and an extended high-frequency tail (top left panel of Figure 1). These profile features suggest that at least three nearly symmetric top profiles (Figure 4) are required to fit the Perseus spectrum, two for the peak region and one for the tail. Since a single symmetric top profile is characterized by three parameters, n, S_p, and ν_p, nine or more (e.g., for a four-profile fit) parameters

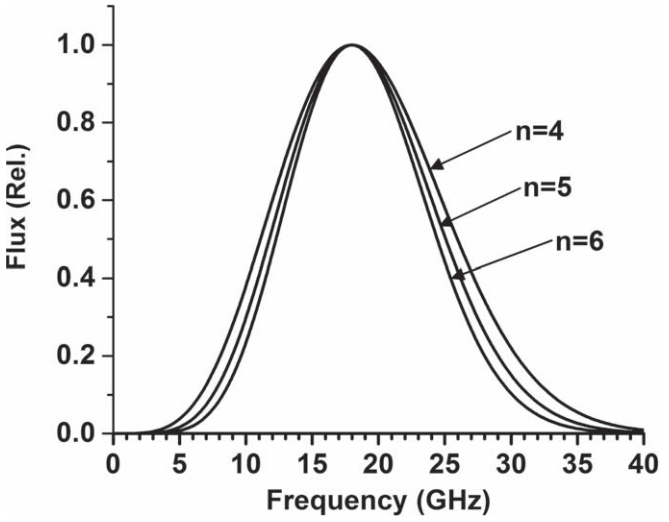

Figure 4. Sensitivity of the analytic AME spectral model (Equation (1)) to the value of n for $\nu_p = 18$ GHz and $S_p = 1.0$. The FWHMs for the curves are 14.82, 13.27, and 12.15 GHz for $n = 4$, 5, and 6, respectively. The curves are for a single carrier at a single $T_{\rm rot}$, where $n = 5$ and 6 correspond to linear and symmetric top carrier geometries, respectively. While we assume that the carriers are symmetric top molecules, $n = 6$, it is convenient to use the lower value of $n = 5$ to simulate the combined spectral broadening effects due to the distributions of carrier sizes and rotational emission temperatures, as well as a non-Maxwellian distribution of the rotational angular momentum (see Appendix C).

are available to fit the noisy 19-data-point Perseus spectrum. The large number of adjustable parameters for a sparsely sampled, noisy spectrum raises issues regarding overfitting and finding plausible parameter constraints to reduce the number of adjustable parameters to a more meaningful level.

We briefly summarize key aspects of the spectral fitting approach (see Appendix B for details). We performed the Perseus fit with a fixed $n = 5$ value for all the symmetric top carrier components (see Appendix C) and varied S_p and ν_p for each contributing profile. A least-squares fitting algorithm was employed that accounted for the uncertainty of each data point. As displayed in Figure 5, we see that two symmetric top profiles provide a very good fit to the observed spectrum. There is no statistically significant improvement associated with adding a third or fourth profile. The fourth component is fitting the noise for the lowest-frequency points clustered around the baseline, which indicates the onset of overfitting the data.

While adding a third profile provides a more visually appealing fit than two profiles, it is not obvious, given the sparse sampling and noise of the tail region data, that this is a statistically meaningful improvement. Applying the statistical F-test to two versus three profiles, we determined a p value of 0.35. Since $p \leqslant 0.05$ would justify adding the two extra fitting parameters associated with the three-profile fit, we conclude that the Perseus spectrum is adequately fit with two profiles. We applied the F-test to the other single-source AME spectra in Figure 1 and find that a two- versus a three-profile fit is preferred in all cases. The p values are presented in Table 1. We did not apply this test to the MWC 297 spectrum since it is fit by a single profile. If future observations establish the existence of a high-frequency tail, then a third model profile would be included in the fitting process. We do not anticipate that the addition of the third profile would substantively impact the key results of this study based on two profiles.

Figure 5 also presents the Perseus fit achieved with the classic spinning dust model, SPDUST.2 (Ali-Haïmoud et al. 2009;

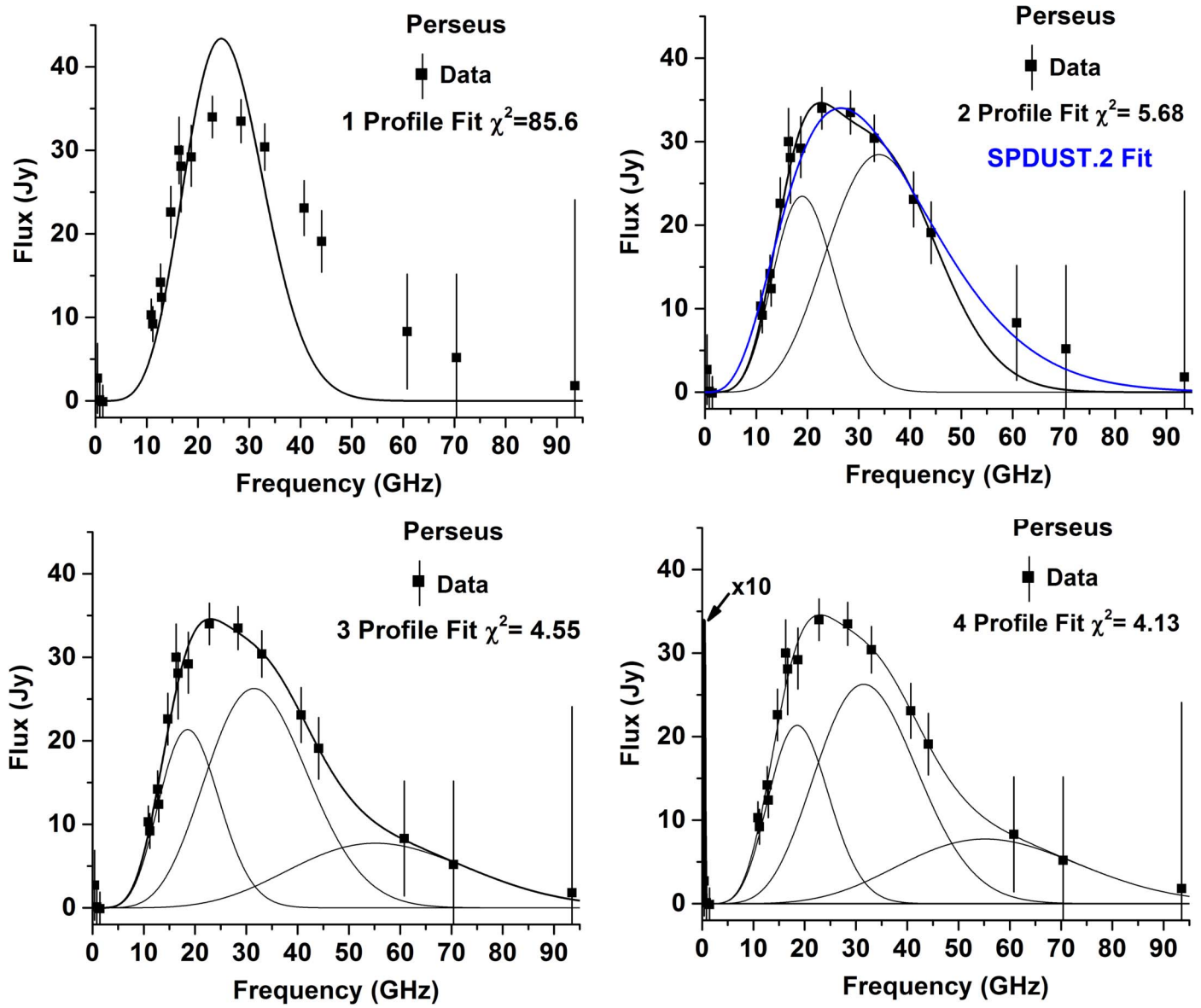

Figure 5. Illustrating the number of carrier component profiles needed to accurately model the Perseus AME spectrum. Each plot shows the overall fit (thick black line) and its individual components (thin black lines). The χ^2 fitting error is indicated for each plot. For the four-profile fit (bottom right panel), the fourth component occurs at ~1 GHz and was multiplied by a factor of 10 for display purposes. Also shown is the SPDUST.2 model fit (blue line in the top right panel; Génova-Santos et al. 2015).

Silsbee et al. 2011). The SPDUST.2 fit captures the general features of the observed Perseus spectrum. However, it lacks some of the finer details, in particular the peak location and the surrounding asymmetric shape. The SPDUST.2 fit utilizes 12 adjustable parameters, $N_{\rm H}$, $n_{\rm H}$, a_0, T_g, $\chi_{\rm H}$, and G_0, for each of two assumed AME environments (Génova-Santos et al. 2015). In comparison, the 2CF model employs four adjustable parameters, S_p and ν_p for each profile, with the assumption that $n = 5$ for both profiles.

3.3. Applying the 2CF Spectral Model to the AME Spectra in Figure 1

Motivated by the fit to the Perseus spectrum, we explored the applicability of the 2CF model to other AME spectra. The fitting procedure involved two steps, where each step used an uncertainty-weighted least-squares algorithm to determine the model parameter values (details in Appendix B). The sources for the data and their uncertainties are detailed in Section 2. With one exception, LDN 1622, the uncertainties used were those referenced in Section 2. For LDN 1622, there are two data points near the emission peak, at 31 (CBI) and 33 GHz (*Wilkinson Microwave Anisotropy Probe*), that possess inconsistent uncertainties (see Figure 1). The intensity difference between these points is much larger than the stated uncertainties, due to the very small error bar (1.3%) on the 31 GHz CBI data point that effectively drives the spectral fit. The error bar is dominated by the absolute calibration uncertainty. Since the flux density was derived using a model for the spatial morphology of the cloud (Casassus et al. 2006), we argue that the true uncertainty should be substantially larger. We therefore use the same uncertainty at 31 GHz as that used for the 33 GHz data point (8%), which then gives approximately equal weight to both data points.

In the first fitting step, the model parameters were initialized by shifting the 2CF Perseus fit to match the spectrum under

Table 1
Spectral Fitting Parameter Values for the Observed AME Spectra for the Fits Displayed in Figures 1 and 2

Source	T_{rot}[a] (K)	$\nu_{p,1}$ (GHz)	$S_{p,1}$ (Rel.)	$\nu_{p,2}$(GHz)	$S_{p,2}$(Rel.)	p[b]
Perseus	21.3	19.0	1.00	34.0	1.21	0.35
LDN 1622	18.5	17.7	1.00	31.7	1.19	0.30
ρ Ophiuchi W	38.7	25.6	1.00	45.6	0.81	0.09
CA Nebula	64.3	33.0	1.00	57.9	1.99	0.55
W44r	16.5	16.7	1.00	32.2	0.96	0.09
W43r[c]	11.4	13.9	1.00	25.3	0.99	
	90.7	39.2	0.63	64.6	0.63	
W47r	18.3	17.6	1.00	29.3	0.93	0.51
G173.6+2.8	22.7	19.6	1.00	39.6	0.68	0.29
NGC 6946	19.3	18.1	1.00	33.5	1.15	0.51
Gould Belt	16.5	16.7	1.0	27.8	0.93	
NGC 4725	50.0	28.8	1.0	58.2	0.68	
MWC 297	146	49.8	1.00			
SMC[c]	663	106	1.00	193	0.99	
	58.6	31.5	0.105	57.3	0.104	
LMC[c]	651	105	1.00	191	0.99	
	87.5	38.5	0.047	70.0	0.047	
⟨AME⟩	21.3	19.0	1.00	34.5	0.99	

Notes. The peak frequencies, $\nu_{p,i}$, and relative peak heights, $S_{p,i}$, for each of the 2CF (i = 1–2) fit components are presented in the last six columns. The peak heights are normalized relative to the peak height of the lowest-frequency (i = 1) component. References to the observations for each source are given in Sections 2.1–2.13.
[a] The rotational temperatures are defined relative to that for LDN 1622, where $T_{\rm rot} = (\nu_{p,1}/17.7)^2 18.5$ K.
[b] p value for F-test of two versus three fitting profiles for the single AME sources in Figure 1.
[c] The two rows for W43r, SMC, and LMC correspond to the fitting parameters for the superposition of two shifted and peak height scaled AME reference spectra, ⟨AME⟩.

consideration. This was accomplished using a single multiplicative parameter applied to the emission frequency scale, $\nu' = \beta\nu$, where ν refers to the Perseus model spectrum. The peak height of the shifted spectrum was also adjusted to best match the spectrum under consideration. In the second step, the peak heights and peak frequencies of the two profiles were independently varied. The resulting fit parameters are presented in Table 1.

Inspection of the Figure 1 fits shows that the 2CF model provides good fits to the less noisy data points below ∼50 GHz. An interesting result is that the majority of the model profiles exhibit similar shapes. That is, the ratios of their component peak heights and peak frequencies vary over a modest range, which we refer to as in-unison variation. The peak height ratio ($S_{p2}/S_{p,1}$) has a mean value of 0.99 and a standard deviation of ±16%. We excluded the CA Nebula from these statistics because its peak height ratio of 1.99 is an outlier according to the Grubbs outlier test, with a 99% confidence level. The peak frequency ratio ($\nu_{p,2}/\nu_{p,1}$) has a mean value of 1.82 and a standard deviation of ±3.8%. We excluded the G173.6+2.8 from these statistics because its peak frequency ratio of 2.02 is an outlier, with a >99% Grubbs confidence level. MWC 297 did not contribute to these statistics because it was fit with a single carrier profile. The origin for in-unison variation of fullerene-based carriers and the larger standard deviation for the peak height ratio are discussed in Section 5.3. The average peak height and peak frequency ratios above are used to define an average AME spectral fit profile, specified by ⟨AME⟩ in Table 1. The ⟨AME⟩ profile was defined using a low-frequency peak location of $\nu_{p,1}$ = 19.0 GHz.

Whether or not the CA Nebula and G173.6+2.8 ratios of peak height and peak frequency outlier values have a physical origin remains to be established. We note that these sources exhibit the largest error bars for the data points below 50 GHz, indicating that the outliers may be a consequence of very noisy data. The mean values for the ratios of the peak heights and peak frequencies serve to define an AME reference spectrum that was used in the fitting of the SMC, LMC, and W43r spectra, as discussed below. The parameters defining the reference spectrum, ⟨AME⟩, are presented in Table 1.

3.4. Applying the 2CF Spectral Model to the Gould Belt and NGC 4725 Spectra

The Gould Belt and NGC 4725 data are very sparsely sampled (i.e., five or fewer data points) over a restricted range of their full AME spectrum. Consequently, applying the four-adjustable-parameter 2CF model to fit a comparable number of data points is questionable. Instead, we decided to determine whether these spectra were consistent with the better-defined spectra in Figure 1. This determination was based on finding a best match between the Gould Belt and NGC 4725 observations and the model fits for the Figure 1 spectra.

The closest match was found by frequency shifting and normalizing each model spectrum to determine the best overlap with the observed spectrum. The frequency shifting was applied using the frequency scale transformation, $\nu' = \beta\nu$, where ν refers to the model fit spectrum from Figure 1. The resulting comparisons in Figure 2 indicate that potentially good matches exist; however, a final determination requires improved observational sampling of the Gould Belt and NGC 4725 AME spectra. The model comparisons predict significant structure that is not captured by the sparsely sampled data, which provides a validation test for the 2CF model.

3.5. Applying the 2CF Spectral Model to the SMC, LMC, and W43r Spectra in Figure 3

3.5.1. SMC and LMC Fits

The SMC and LMC warrant special consideration because their emission spectra occur at much higher frequencies than

the classic AME spectra discussed above. Like W43r, the SMC and LMC spectral fits require two ⟨AME⟩ reference spectra (see Figure 3). However, unlike W43r, the two reference components for SMC and LMC have very different relative peak intensities. The relatively high peak frequencies for the two dominant SMC and LMC fit components correspond to much higher rotational temperatures than are typical for AME spectra. The rotational temperatures for the two fit components for each observed spectrum are $T_{\rm rot} = 663$ and 59 K for SMC and $T_{\rm rot} = 651$ and 88 K for LMC.

Bot et al. (2010) obtained good fits to the SMC and LMC spectra using the Draine & Lazarian (1998a, 1998b) spinning dust model. The fits required two very different environments, the diffuse ISM and a PDR. They considered a range of PDR environments with gas temperatures that encompass the higher rotational temperatures (i.e., 651 and 663 K) we determined. The PDR densities ranged from $n_{\rm H} = 10^3$ to $10^5\,{\rm cm}^{-3}$, for which the rotational and gas temperatures may be equilibrated, as discussed in the following section.

An interesting result of our analysis is that the LMC and SMC spectra are predominantly fit by a single reference spectrum. This result is surprising because the observed spectra were spatially integrated over large areas, of order 900 pc. One would expect that the observed averaged spectra would reflect the contribution of multiple diverse sources, resulting in a wide distribution of $T_{\rm rot}$ values. If this were the case, the observed spectra should be broader than the width of a single reference spectrum. We discussed earlier that the 2CF model could accommodate a distribution of $T_{\rm rot}$ values corresponding to as much as $\sim\pm22\%$ of the average value. This spread in $T_{\rm rot}$ values corresponds to $\sim\pm120$ K for the SMC and LMC observations.

Several alternative models have been proposed to explain the LMC and SMC high-frequency excess emissions. Draine & Hensley (2012) demonstrated that a mixture of electric dipole emission from small dust grains and magnetic dipole emission from small ferromagnetic dust grains provided a good fit to the LMC and SMC data. The two-level system (TLS) solid-state emission model of Meny et al. (2007) has also been considered (Planck Collaboration 2011a). However, the TLS model could not reproduce the spectral shape of the SMC spectrum. Polarization measurements of the excess high-frequency emission could clarify the potential contribution of magnetic dust grains (Draine & Hensley 2012).

3.5.2. W43r Fit

The unusual breadth of the W43r spectrum is apparent in Figure 3. It is much broader than a single reference spectrum. The observed W43r spectrum is reasonably fit as a sum of two shifted ⟨AME⟩ reference spectra. The rotational temperatures for the two fit components are $T_{\rm rot} = 11.4$ and 90.7 K (Table 1). The lower temperature is interesting because it is typical of protostellar cold cores. The 11.4 K rotational temperature may be associated with one of the dense protostellar clumps in W43, and it is consistent with the measured range of CO rotational temperatures of $T_{\rm rot} = 5$–18 K (Luong et al. 2011). It has proven difficult to observe AME in a protostellar cold core, with only a single, tentative detection (Tibbs et al. 2015a, 2015b). The high-temperature reference spectrum is comparable to that for the CA Nebula and could arise from a similar source, such as a PDR.

4. Carrier Size Estimation and Rotational Temperature Predictions

4.1. Carrier Size Estimation

The key to obtaining a good estimate of a carrier's size is to obtain a good estimate of its rotational emission temperature. This task is simplified for certain interstellar environments, in particular for a DC. We quantify below that for a DC the relationship $T_{\rm rot} \approx T_K$ is a valid approximation. Harper et al. (2015) attributed the AME source for the LDN 1622 to a DC with $T_K = 22$ K (Harper et al. 2015). In an earlier analysis of the LDN 1622 AME spectrum, Iglesias-Groth (2006) used a gas temperature of $T_K = 15$ K. These gas temperatures fall within the typical temperature range of 10–30 K for a DC (Scaife 2013).

For the purpose of estimating the carrier sizes, we take $T_{\rm rot} = 18.5$ K, which is the average of the LDN 1622 temperature range mentioned above. Using Equation (3) with $T_{\rm rot} = 18.5$ K, $n = 5$, and the ν_p values for LDN 1622 in Table 1, we obtain *effective/average* rotational constants for the two carrier components of 0.0027 and $0.0087\,{\rm cm}^{-1}$. The uncertainty in the derived rotational constants is primarily determined by that for $T_{\rm rot}$, which is $\pm19\%$ (i.e., ±3.5 K). The derived rotational constants correspond to the fullerenes C_{60} and C_{34} of 0.0028 and $0.0087\,{\rm cm}^{-1}$, respectively. C_{60} is the most stable fullerene, and it is plausible that one of the derived rotational constants corresponds to that for C_{60}. On the other hand, C_{34} is less stable than its comparably stable neighbors C_{32} and C_{36} (Kroto 1987; Kietzmann et al. 1998). An equally abundant mixture of C_{32} and C_{36} would result in an average rotational constant equivalent to that for C_{34}. As subsequently discussed, the two carrier families correspond to a distribution of similarly sized fulleranes, where the family associations with C_{60} and C_{36} reflect the most stable parent fullerene for each family.

We characterize the size and temperature distributions for the carrier families, which, for our spectral model, are determined by the fitting parameter n. As presented in Appendix C, the spectral fitting results are relatively insensitive to the value of n. We adopted $n = 5$ because it produced a slightly better fit to the Perseus spectrum. A good fit was obtained for $n = 6$, which corresponds to the limit of a single symmetric top molecule giving rise to each of the two components. However, we suggest that it is more likely that each component is composed of a distribution of similarly sized molecules. The extra width can be represented as additional profiles that are shifted with respect to the parent profile. The shift was modeled in terms of a variation of the carrier rotational constant or temperature, or a combination of the two. We use Equation (3) to relate the increased widths for $n = 5$ or 4 to a distribution of carrier sizes and rotational temperatures. The relationship is given by $\Delta(BT_{\rm rot})/BT_{\rm rot} = \pm\Delta\nu/\nu_p$, where B, $T_{\rm rot}$, and ν_p refer to the parent carrier values and $\Delta\nu$ is the increase in profile width relative to that for $n = 6$. From the values of $\Delta\nu$ given in Figure 4, we obtain $\Delta(BT_{\rm rot})/BT_{\rm rot} = \pm9$ and $\pm22\%$ for $n = 5$ and 4, respectively. These excursions from the single carrier approximate a 1σ deviation for either B or $T_{\rm rot}$, assuming that only one parameter varies. For the C_{60} carrier family, this translates into a size variability of $\Delta N_{\rm C} = \pm3$ and ±7 (i.e., $N_{\rm C} \propto B^{-1/2}$ for a PAH or fullerene) for $n = 5$ and 4, respectively. For the case of $n = 4$, the size distribution could accommodate carriers in a size range of up to $N_{\rm C} \sim 50$–70. For

$T_{\rm rot}$, the variations can be as large as $\Delta T_{\rm rot} = \pm 1.7$ and ± 4 K for $n = 5$ and 4, respectively.

While we have associated the derived B values with spherical top fullerenes in the $N_{\rm C} = 20$–60 size range, similar results are obtained if we assume, for example, oblate top molecules (i.e., compact PAH). This yields PAHs in the $N_{\rm C} = 18$–54 size range. We find that the size range of the AME carriers is well established apart from specific knowledge of the carrier type and geometry.

4.2. Theoretical Predictions of T_{rot} for Different Interstellar Environments

Rigorous modeling of the rotational excitation for all the interstellar environments that may produce AME is a challenging problem. Our objective in this section is more limited. We seek to understand under what environment conditions the approximation $T_{\rm rot} = T_K$ is valid. The primary environment parameter controlling the effective rotational temperature is the collision rate, which is proportional to the ambient density.

We use the Oka model (Oka et al. 2013) to quantify the dependence of $T_{\rm rot}$ on the environment and molecular parameters that are most important for DC, MC, translucent cloud (TC), and CNM environments. We assume that the carriers are neutrally charged and that their dominant collisions are with H and H_2. The assumption of neutral carriers, for the aforementioned environments and for $N_{\rm C} < \sim 70$, is supported by the Weingartner & Draine (2001b) grain-charging model. Furthermore, there is currently no compelling observational evidence that AME arises from environments with large H^+ mole fractions (Planck Collaboration 2011b; Dickinson et al. 2018). The model includes collisional and radiative excitation and relaxation and radiative pumping by the CMB. While the model was formulated for linear molecules, we assume that it is reasonably applicable to symmetric top molecules. The end-over-end tumbling (i.e., the emitting motion) of a symmetric top is analogous to the rotation of a linear molecule.

There are three model inputs, the dipole moment, the rotational constant, and the rotation collisional excitation rate for a single quanta excitation, $J \rightarrow J + 1$, $C_{J,J+1}$. The latter is computed from

$$C_{J,J+1} = \sigma v n_{\rm H_2}, \tag{4}$$

where σ is the collision cross section, v is the mean collision velocity, and $n_{\rm H_2}$ is the number density of H_2. For environments in which the hydrogen is in its atomic form, the appropriate substitutions of $n_{\rm H}$ and $m_{\rm H}$ need to be made in the above and following expressions. We did not include a modest He contribution, which would increase $C_{J,J+1}$ by ~17%–35%, depending on whether H or H_2 was the dominant species, respectively. The rotation collisional de-excitation rate (i.e., $J \rightarrow J - 1$) is calculated assuming detailed balance (Oka et al. 2013). Because translation to rotation energy transfer is efficient, we take the rotational energy transfer cross sections to be equal to the collisional cross section. We show below that this assumption yields comparable rotational energy transfer rates to those estimated by Oka et al. (2013) for similar interstellar conditions.

The cross section is approximated as the total elastic cross section for the attractive component of the Lennard-Jones 6–12 potential (i.e., the $1/r^6$ term; Rothe & Bernstein 1959). This is an appropriate limit for low-velocity collisions between species with an attractive potential, as is the case here for a neutral carrier colliding with the dominant neutral ISM species (i.e., H, H_2, and He). The cross section is calculated using

$$\sigma = b_0 \left(\frac{2\varepsilon r_m^6}{v} \right)^{2/5}, \tag{5}$$

where b_0 is a constant (4.662×10^{11} in cgs units; Rothe & Bernstein 1959), ϵ is the depth of the potential well, and r_m is the separation between collision pairs at the potential minimum. For fullerene carriers, the potential parameters ϵ and r_m are approximated by those for the interaction of H and H_2 with a graphite surface (Jeloaica & Sidis 1999; Sun et al. 2007). Theoretical studies show that the interaction potentials for H_2 with coronene ($C_{24}H_{12}$) and an infinite 3D graphite surface are nearly the same (Sun et al. 2007). Hence, we use the same potential parameters for the range of fullerenes under consideration, C_{20}–C_{60}. The potential parameters are $\epsilon = 0.07$ eV and $r_m = 3.0$ Å for H_2 and $\epsilon = 0.07$ eV and $r_m = 2.8$ Å for H. Evaluation of Equation (5) using these parameter values and a typical collision velocity of $v \sim 5 \times 10^4$ cm s^{-1} for $T_K = 20$ K results in a collision cross section of 5×10^{-14} cm^2. For reference, this cross section is an order of magnitude larger than those based on hard sphere collisions. Several additional contributions to the cross section, not included here, could increase the cross section by up to a factor of two. These include the radius of a fullerene (i.e., the interaction potential is based on the distance from a surface) and the dipole–induced–dipole interaction between a polar carrier and the nonpolar ambient species.

The mean collision velocity is calculated from

$$v = \left(\frac{8kT_K}{\pi m_{\rm H_2}} \right)^{\frac{1}{2}}, \tag{6}$$

where $m_{\rm H_2}$ is the mass of H_2. For H_2 at $T_K = 20$ K, the velocity is $v = 4.60 \times 10^4$ cm s^{-1}.

Given the preceding characteristic values for the collision cross section and velocity, the characteristic collision rate for a DC with $n_{\rm H_2} = 10^4$ cm^{-3} is $C_{J,J+1} = 2.5 \times 10^{-5}$ s^{-1}. Oka et al. (2013) estimated a rate of $C_{J,J+1} = 1 \times 10^{-7}$ s^{-1} for a lower density, $n_{\rm H_2} = 10^2$ cm^{-3}, and higher temperature, $T_K = 100$ K. Scaling our rate to Oka's conditions yields $C_{J,J+1} = 1.3 \times 10^{-7}$ s^{-1}, which agrees well with Oka's estimate of $C_{J,J+1} = 1 \times 10^{-7}$ s^{-1}. To put this rate into perspective, it is some two orders of magnitude faster than the typical rate for radiative relaxation for the proposed carriers (see Appendix A). Consequently, in a DC the rotational temperature is in equilibrium with the gas kinetic temperature, $T_{\rm rot} = T_K$.

Figure 6 summarizes the computed $T_{\rm rot}$ values using Oka's model for a wide range of ISM environments. Each plot is for a specific ISM environment, characterized by a representative gas kinetic temperature, T_K, and an H or H_2 number density, $n_{\rm H}$ or $n_{\rm H_2}$. The $T_{\rm rot}$ values are plotted as a function of the parent fullerene rotational constant, B, for a fixed dipole moment, μ. As discussed later, the range of dipole moments considered, 0.2–1.6 D, corresponds to possible dipolar fullerene variants (Appendix D), such as a fullerane or a caged Fe atom.

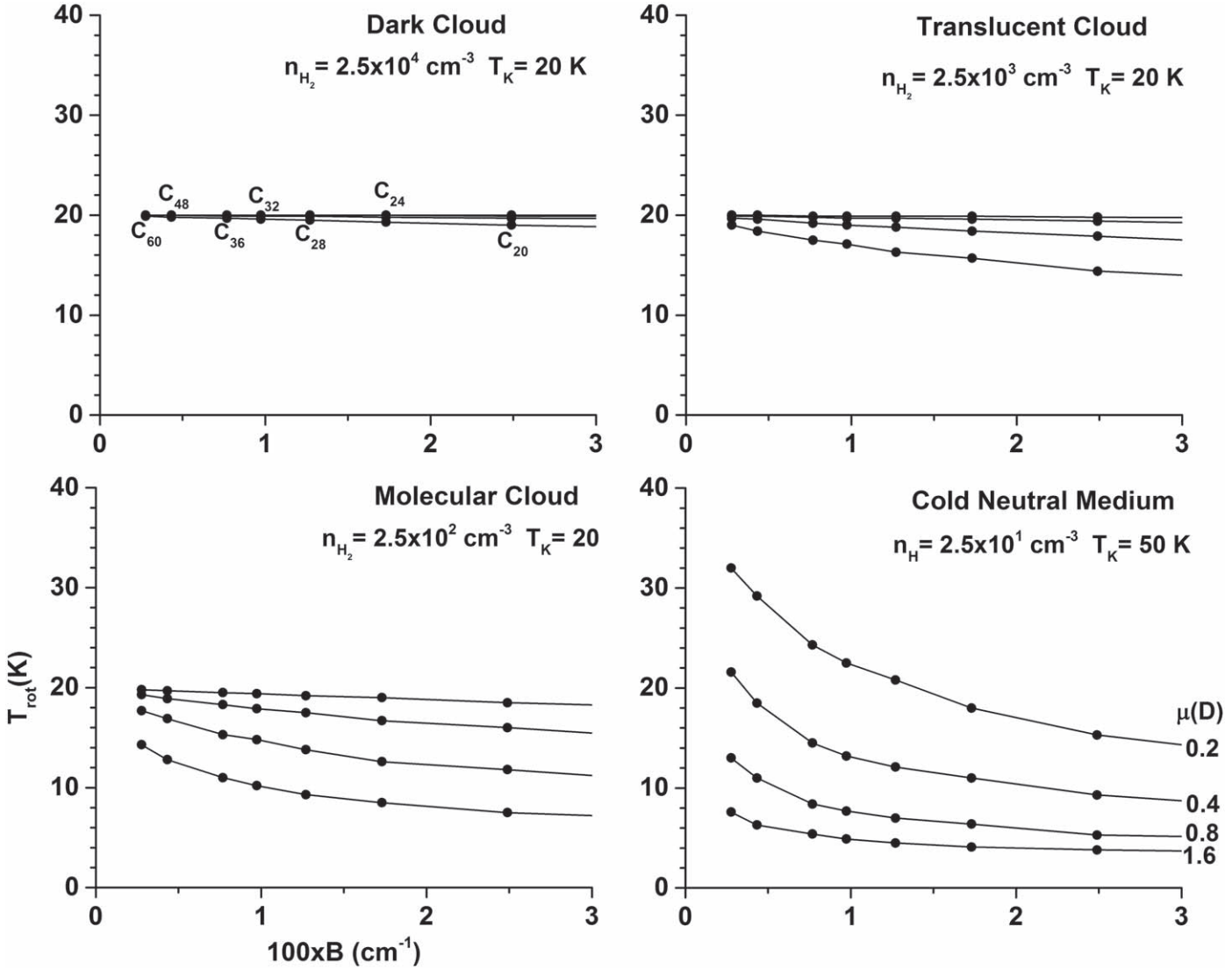

Figure 6. Calculated effective rotational temperatures, $T_{\rm rot}$, based on the Oka et al. (2013) kinetic excitation and relaxation model with neutral–neutral collision cross sections determined by a $1/r^6$ interaction potential (see Equation (5)) and for different representative neutral ISM environments (Draine & Lazarian 1998b; Snow & McCall 2006). The calculations are for fullerene analogues with sizes, C_{20}–C_{60}, as indicated in the top left panel. Each of the panels displays four curves corresponding to different dipole moments, as denoted in the bottom right panel.

4.3. Implications of the T_{rot} *Predictions for the 2CF Spectral Model Data Fits*

A key result drawn from the model calculations in Figure 6 is that, for a DC, $T_{\rm rot} = T_K$ is a valid approximation for all the B values, regardless of the value of the dipole moment. This implies that the B value inferred for the lowest-frequency fit component for the LDN 1622 spectrum is well determined. Our identification of the carrier as C_{60} was motivated by the proximity of the derived B value to that for C_{60}, as well as chemical considerations elaborated later.

Another important inference gleaned from Figure 6 is that for an identical dipole moment for all the fullerene carriers, the rotational temperatures for the different rotational constants do not vary in unison (i.e., maintain the same proportionality) for changes in the environmental properties. In order to obtain an in-unison variation, a trend deduced from the spectral analysis, the dipole moment needs to decrease with increasing B.

We explore the in-unison idea in more detail. The Figure 6 predictions imply that in-unison rotational temperature variations can be attained for the considered environments if the dipole moment for the C_{60} component is about 40% larger than that for C_{36}. For these dipole moments, $T_{\rm rot}$ will be approximately constant for the two carrier components, to within ± 1 K for all the environments. However, as the density becomes lower, and radiative relaxation becomes much faster than collisional excitation and relaxation, we expect the constant $T_{\rm rot}$ behavior to eventually break down.

We note that the environmental conditions explored in Figure 5 are representative of each environment and that there is considerable variability of these parameters within each environment. For example, for an MC, T_K can range from $\sim$20 to 100 K and $n_{\rm H}$ from $\sim$100 to 500 cm^{-3} (Snow & McCall 2006). This means that the CA Nebula, for which $T_{\rm rot} \sim 65$ K, while seemingly an AME outlier, can plausibly be explained in terms of the upper ranges of $T_{\rm rot}$ and $n_{\rm H}$ for an MC. We note that these conditions are also comparable to those for a PDR (Bot et al. 2010), which is the speculative source for the CA Nebula (Planck Collaboration 2014).

We have not included a PDR in our survey of environments presented in Figure 6. However, we note that PDR properties significantly overlap with those for the MC, TC, and DC environments. Typical PDR property ranges include $n_{\rm H} = 10^3$–$10^5\,{\rm cm}^{-3}$, $T_K = 50$–$1200\,{\rm K}$, and low to high ionization fractions (Bot et al. 2010). For the high range of PDR densities, $n_{\rm H} > 10^4\,{\rm cm}^{-3}$, the assumption that $T_{\rm rot} = T_K$ should be valid.

5. Discussion

5.1. Key Result

The key result of this investigation is that a spectral model composed of two carrier families yields good fits to a diverse collection of 14 galactic and extragalactic AME spectra. Eleven of the spectra arise from a single dominant source (Figure 1) and, with one exception, are fit with two carrier families. The exception is MWC 297, which is fit with a single carrier family. The other three spectra arise from two sources (Figure 3) and require a superposition of two shifted 2CF spectra to obtain a good fit.

The key result is valid irrespective of whether or not our identification of the carriers as fullerene-based molecules is correct. It applies to any of the most likely carrier types, including PAH molecules, fulleranes, and very small grains.

The subsequent subsections explore various issues arising from the fullerane carrier hypothesis.

5.2. Productions and Stability of Fullerenes in the ISM

We consider the viability of fullerene-based AME carriers with respect to their lifetimes in the ISM. A key measure of molecular lifetime in the ISM is the timescale for UV photodissociation. We briefly overview a postulated formation mechanism for large molecules in the ISM, followed by a discussion of the UV photostability of fullerenes and fulleranes.

5.2.1. Fullerene Production

The formation mechanisms for fullerene and PAH molecules are uncertain (Berné & Tielens 2012; Berné et al. 2015; Cami et al. 2018; Candian et al. 2018b). However, their photodissociation pathways and rates are better characterized (Allain et al. 1996; Berné & Tielens 2012; Berné et al. 2015). Fullerenes are more resistant to UV photodissociation than PAH molecules of comparable size (Berné et al. 2015). As discussed below, the extraordinarily long lifetimes of fullerenes, C_{60} in particular, signify that fullerene-based molecules may be significant AME carriers.

Large carbonaceous molecules, such as fullerenes and PAHs, are formed in the carbon-rich envelopes of evolved stars, and they are eventually expelled into the ISM (Berné & Tielens 2012; Berné et al. 2015; Cami et al. 2018; Candian et al. 2018b). It is conjectured that their formation involves "top-down" chemistry in which dust grains and high-intensity UV radiation fields interact to spawn large grapheme sheets. The grapheme sheets are further processed via photodissociation, fragmenting to smaller sheets, which can fold to form fullerenes or become hydrogenated to form PAH molecules. We focus here on the lifetimes of the fullerenes once they are injected into the ISM and subsequently populate the various environments associated with AME.

5.2.2. Fullerene and Fullerane Stability

We estimate the photodissociation timescales for the two parent fullerenes in different environments. Berné et al. (2015) modeled a photodissociation timescale for C_{60} of about $3 \times 10^{12}\,{\rm s}$ for a UV radiation field of $G_0 = 2 \times 10^5$ (estimated from their Figure 5), which translates into a timescale of $\sim 2 \times 10^{29}\,{\rm s}$ for the standard UV radiation field of $\chi_{\rm UV} = 1$ ($\chi_{\rm UV} = 1.7 G_0$; Draine 1978). Rapid photodissociation of C_{60} occurs at an internal energy of $\sim$35 eV, which requires the near simultaneous absorptions of three $\sim$11.7 eV UV photons. The $\chi_{\rm UV} = 1$ photodissociation timescale corresponds to 6×10^{15} Myr, which is much greater than the current age of the universe, 1.4×10^4 Myr. Hence, C_{60} is virtually indestructible and, once produced, will accumulate over time. Nevertheless, there are a few environments capable of photodissociating C_{60} on a faster timescale. One is in the vicinity of a star, where $\chi_{\rm UV} = 10^5$ or larger (Berné et al. 2015), for which the photodissociation timescale is lowered to $6 \times 10^{15}/(10^5)^3 = 6$ Myr.

Destruction processes other than photodissociation may further limit the lifetimes of C_{60} and the other fullerenes in the ISM. For instance, if we view C_{60} as a small dust grain, then energetic collisions in interstellar shocks would limit its lifetime to $\sim$600 Myr (Jones et al. 1996). Destruction of C_{60} from dissociative collisions with energetic cosmic rays could result in comparable lifetimes. Collisions with high-energy electrons lead to ejection of a single C atom, while collisions with energetic ions, such as H^+ and $He,^+$ lead to ejection of a C_2 molecule. The threshold energies for these processes are approximately 15 eV (theoretical model for grapheme in Krasheninnikov & Nordlund 2010) and 11 eV (experimental value in Głuch et al. 2004) for electron and ion collisions, respectively. Based on the cosmic-ray processing model of Micelotta et al. (2011), these thresholds correspond to C_{60} lifetimes in the range of $\sim$100–1000 Myr for representative spiral and starburst galaxies.

In order to estimate the photodissociation timescale, $\tau_{\rm dis}$, for C_{36}, we need to establish (1) the number of absorbed UV photons required for dissociation, (2) the timescale for absorption of a single photon, τ_1, and (3) the timescale for radiative cooling of the energy deposited by an absorbed UV photon, $\tau_{\rm IR}$. We estimate the number of UV photons required for dissociation by assuming that temperatures required for efficient dissociation of C_{36} and C_{60} are comparable. C_{60} dissociation proceeds quickly at 35 eV, which corresponds to an internal temperature of about 3000 K, as determined by integration of the temperature-dependent heat capacity. For C_{36}, an internal temperature of 3000 K corresponds to an energy of 20.8 eV; thus, C_{36} photodissociation requires, on average, two 10.4 eV photons, as compared to three 11.7 eV photons for C_{60}. The timescale for single photon absorption is determined by integration of the product of the spectral UV flux for $\chi_{\rm UV} = 1$ (Draine 1978) and absorption cross section over the energy range of 10.4–13.6 eV (the upper bound imposed by the Lyman limit). We take the C_{36} absorption cross section to have the same spectral profile as that for C_{60} (Berkowitz 1999), but lower by a factor of 0.5 in absolute value (Koponen et al. 2008). The resulting timescale for single photon absorption is $\tau_1 = 2.3 \times 10^8\,{\rm s}$. The timescale for infrared radiative cooling was estimated based on a density function theory (DFT) calculation (see Appendix D) of the vibrational frequencies and Einstein A-coefficients and

an internal temperature of 1800 K, which corresponds to the absorption of a single 10.4 eV photon. The resulting timescale for infrared radiative cooling is $\tau_{IR} = 0.17$ s for the loss of 1 eV of internal energy.

The photodissociation timescale for a molecule requiring the near-simultaneous absorption of two UV photons is estimated using

$$\tau_{dis} = \left(\frac{\tau_1}{\chi_{UV}}\right)^2 \frac{1}{\tau_{IR}}. \quad (7)$$

For C_{36} with $\chi_{UV} = 1$, we estimate $\tau_{dis} = 4 \times 10^3$ Myr. C_{36} is predicted to be extremely stable for UV intensities of $\chi_{UV} < 1$ (i.e., lifetime similar to the current age of the universe), which may pertain to most of the AME observations. In this limit, we would expect the relative abundances of C_{60} and C_{36} to remain fairly constant. For higher UV fields, the C_{36} component should eventually diminish relative to C_{60}. The C_{36} component appears to be absent in MWC 297, which is consistent with the extremely intense UV field for its Herbig Ae/Be star (Section 5.6).

We expect that a fullerane's lifetime will be longer than that for its parent fullerene, because a fullerane can also dissipate absorbed UV energy by breaking C–H bonds. The C–H dissociation energies for fulleranes are relatively low, 3.6 and 2.1 eV for C_{36} and C_{60}, respectively (Appendix D). These bond energies are small enough to allow two C–H bonds to be severed by absorption of a single 11 eV photon (estimated using Equation (3) in Berné & Tielens 2012). For comparison, the C–H for a PAH is much higher, ~4.8 eV (Montillaud et al. 2013); consequently, only a single C–H bond can be broken for sizes below $N_C \sim 30$ (Allain et al. 1996). The bond breaking energy dissipation mechanism means that an additional UV photon absorption may be required to break the carbon skeleton of the underlying parent fullerene. The increase in the photodissociation timescale due to hydrogenation will depend on the hydrogenation level.

The estimated lifetimes for the parent fullerene carriers are qualitatively consistent with the 2CF fits to the AME observations. The AME-derived relative abundances for the C_{60} and C_{36} families for Perseus were determined to be 1.0 and 0.33, respectively (Section 5.5). We found that the relative peak heights of the C_{60} and C_{36} fit components were approximately constant for most of the observations. In contrast, the existence of a third, high-frequency family, which would correspond to a C_{20} parent carrier, is questionable. This is consistent with the very short predicted lifetime for C_{20} of 4×10^{-6} Myr for $\chi_{UV} = 1$, which corresponds to the absorption of a single photon. The predicted lifetime is so short, even for the moderate UV flux of $\chi_{UV} = 1$, that one would not expect to see a C_{20} component. If the existence of the C_{20} family were eventually established, it would imply that there is a significant, as yet unidentified, source contribution. It is unlikely to arise from photodissociation of the larger fullerenes, since their photodissociation timescales are very long. A potential source term could originate from "bottom-up" chemistry, which is known to produce somewhat smaller observed molecules, in the size vicinity of $N_C \sim 12$ (Herbst 2017).

5.3. Fullerene Hydrogenation Levels and the Origin of In-unison Scaling

The ratios of the fitted peak heights and peak frequencies for the C_{60} to the C_{36} carrier families, for most sources, vary over surprisingly small ranges, ±16% and ±3.8% (Section 3.3), given the large variation in source environments. We explore fullerene hydrogenation as a possible origin for the approximate in-unison scaling of the C_{60} and C_{36} carrier families. We first consider the relationship between dipole moment, peak height, and hydrogenation fraction for the 2CF model. Afterward, we address the problem of modeling the hydrogenation fractions for different environments.

We model the dipole moments and relative peak heights of the fullerene families using a Monte Carlo simulation of the distribution of C–H bonds on a fullerene surface. For a fixed number of C–H bonds, N_{CH}, we sampled their possible arrangements on a fullerene surface. For each configuration, we determined the total dipole moment, μ. The AME peak height is proportional to the average of the dipole moment squared, $\langle\mu^2\rangle$, for the sampled configurations. For each parent fullerene, C_{60} and C_{36}, we attached the H atoms to the known C atom locations for the ground-state fullerene geometries. We note that the peak height depends on several other parameters, $S_p \propto N_H \chi_{ful} \mu^2 \nu_p^n$ (Appendix A); however, our focus in this section is on hydrogenation because of its strong effect on the peak height through the μ^2 factor. Before presenting the simulation results, we describe key simplifications made to the underlying physics.

We assume that the rates per C atom for attaching and for photodissociating H atoms are independent of molecular position and size (Berné & Tielens 2012). Then, the average steady-state hydrogenation per unit area is the same for all the fullerenes. Each C–H bond is taken to contribute a dipole moment of the same magnitude, μ. We also presume that AME arises from environments dominated by neutral fullerene-based carriers.

The assumption of a size-independent photodissociation rate per C atom for breaking a C–H bond seems, upon first consideration, unphysical. For clarity, we distinguish between two different dissociation rates associated with this issue. One is the photodissociation rate, which refers to the overall rate of fullerane dehydrogenation and is controlled, in part, by the UV absorption rate per C atom. The other is the instantaneous dissociation rate, which refers to the much faster rate at which a C–H bond is broken in a vibrationally hot fullerane. If two differently sized fulleranes absorb a UV photon of equal energy, then the energy redistribution process would result in different internal temperatures. This would lead to different instantaneous dissociation rates for the C–H bonds of the two vibrationally hot molecules. However, the photodissociation rate is controlled by the probability of breaking a C–H bond per absorbed UV photon. The dissociation probability is independent of the instantaneous dissociation rate of the hot molecule, as long as the instantaneous dissociation rate exceeds the IR radiative cooling rate (i.e., a dissociation probability of unity). We discussed earlier (Section 5.2.2) that the relatively weak and different C–H bond energies for C_{60} and C_{36} based fulleranes (i.e., 2.1 and 3.6 eV, respectively) would, upon absorption of an 11 eV photon, result in the severing of two C–H bonds for each fullerane. Hence, for these fulleranes, their photodissociation probabilities per absorbed UV photon are equal and are given by the UV absorption rate per C atom.

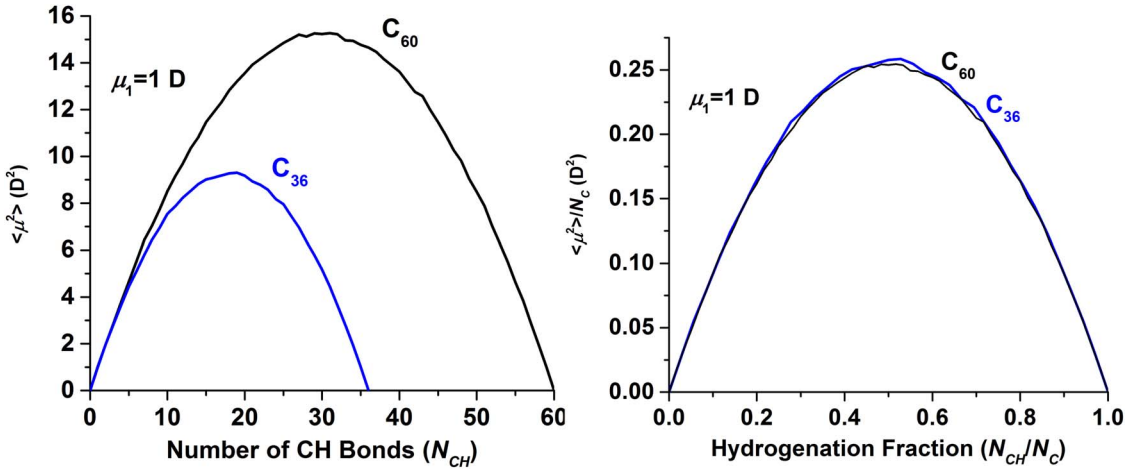

Figure 7. Left panel: simulation results for the dipolar contribution to the AME peak heights, $\langle \mu^2 \rangle$, for different parent fullerenes as a function of the number of C–H bonds, $N_{\rm CH}$. The simulations are for a C–H dipole moment of $\mu_1 = 1$ D. The AME intensities for other values of the C–H dipole moment can be obtained by multiplying the simulated curves by μ_1^2. Right panel: simulation results where both the AME intensity and the hydrogenation levels have been normalized to $N_{\rm C}$ for each fullerene. The minor differences and fluctuations near the peaks are attributed to quantization of site locations and sampling statistics.

The simulation results are displayed in Figure 7. The simulation predicts that the peak heights for the C_{60} and C_{36} components should vary in unison. The simulation did not take into account that the observed intensity for each family is also proportional to its abundance, which may account for the larger standard deviation found for the ration of peak heights. However, the extraordinary stabilities of C_{36} and C_{60} suggest that their relative abundances should remain approximately constant for most environments exhibiting AME.

The simulation also supports the observation of in-unison scaling for the peak frequencies. In Section 4.3, we found that for this frequency scaling to apply, the effective $T_{\rm rot}$ must be the same for each carrier family in a given environment. We discussed that if the effective dipole moment for each carrier family is approximately proportional to carrier size, $N_{\rm C}$, then a nearly constant $T_{\rm rot}$ behavior could occur. The results of this section imply an intensity-weighted effective dipole moment scaling of $N_{\rm C}^{1/2}$, which is consistent with the notion of an approximately constant effective $T_{\rm rot}$ across different environments.

The simulation results imply an upper limit to the observed peak heights given by $(N_{\rm C}/4)\mu_1^2$, corresponding to a 50% hydrogenation level. As quantified later (Appendix E), the upper limit intensity leads to a lower limit for the AME-derived fullerane abundances. The lower intensity limit is zero, which occurs for $N_{\rm CH} = 0$ (no hydrogenation) and $N_{\rm CH} = N_{\rm C}$ (complete hydrogenation). This intensity limit does not place an upper bound on the fullerene abundance because $\mu = 0$ for both hydrogenation levels, and hence AME cannot occur. Clearly, for sources in which AME is observed, some population of polar molecules must exist, but, as discussed below, quantification of this population for different environments is challenging.

5.3.1. Modeling Hydrogenation Levels

The explanation for in-unison scaling does not require explicit knowledge of the actual distribution of hydrogenation levels for a particular environment. In contrast, modeling the absolute AME intensities requires prediction of the hydrogenation levels. Modeling fullerene hydrogenation for different environments is beyond the scope of this study, as can be appreciated by considering the detailed hydrogenation model for PAH molecules developed by Montillaud et al. (2013). Moreover, there are fundamental differences, briefly enumerated below, in the hydrogenation chemistry between fullerene and PAH molecules.

When an H atom attaches to a fullerene C atom, it disrupts the local aromatic character (i.e., a C=C double bond is broken in order to form the C–H bond), whereas the aromatic character of a PAH is independent of the number of attached H atoms. Furthermore, there is likely a modest potential energy barrier, ~0.2 eV, or equivalently ~2200 K, to the formation of a C–H bond for a fullerene, which may substantially lower the reaction rate for environments with low gas kinetic temperatures (e.g., $T_K \sim 100$ K; Jeloaica & Sidis 1999). Proper treatment of this problem also requires consideration of H atom tunneling through a potential energy barrier. In contrast, it is assumed that there is no potential energy barrier for the formation of a C–H bond for a PAH (Berné & Tielens 2012). As mentioned earlier, the smaller C–H bond energies for C_{36} and C_{60} versus a PAH allow two C–H bonds to be severed for the absorption of a single ~11 eV UV photon.

An interesting result of the PAH hydrogenation models is that the state of partial hydrogenation occurs for a limited range of ISM environments, implying that AME may only occur in these environments (i.e., AME requires a dipole moment). We anticipate that the range of environments capable of supporting AME for fulleranes will be somewhat broader because of steric effects that can "stretch" the transition from fully dehydrogenated to fully hydrogenated. The steric hindrance factors, peculiar to a spherical molecule, significantly reduce the H attachment rate relative to that for a PAH. These factors include the following: (1) a surface C atom receives 0.25 of the H atom flux of that for a gas-phase C atom, and (2) as the fractional hydrogenation becomes large, an exposed C atom can be completely surrounded by C–H bonds, which may block ~50% of incoming H atoms from reaching the available C atom.

Finally, the current PAH hydrogenation models are largely focused on attachment of H atoms to peripheral C atoms. The possibility of superhydrogenation is approximately represented by allowing for the attachment of one extra H

atom to the interior of a fully hydrogenated PAH. Superhydrogenation of a PAH is chemically similar to fullerane hydrogenation. Recent progress on understanding the chemistry of PAH superhydrogenation is directly relevant to development of a fullerene hydrogenation model (Rauls & Hornekær 2008; Jensen et al. 2019).

In summary, most of the above differences between fullerene and PAH hydrogenation point toward less efficient hydrogenation chemistry for fullerenes.

5.4. Nondetection of AME Rotational Line Structure for Perseus

Symmetric top molecules exhibit regularly spaced AME emission lines, which enhance their detectability through the use of a spectral comb filter. A comb filter consists of a sequence of regularly spaced, spectrally narrow detection windows. Ali-Haïmoud (2014) and Ali-Haïmoud et al. (2014) demonstrated that a comb filter could be used to selectively and sensitively detect the regularly spaced emission lines for individual, highly symmetric (i.e., low asymmetry parameter) PAH molecules. They conducted high spectral resolution observations in the peak emission region, 23.5–26.6 GHz, of the Perseus AME spectrum. The result from their measurements set an upper bound of 0.001 for the relative abundance of any symmetric top carrier.

We show that the numerous isomers formed by fullerene hydrogenation can explain the null detection result for the Perseus observations. We focus on the isomers of C_{36} and C_{60}, since they are the dominant contributors to the AME spectrum in the 23.5–26.6 GHz spectral window (Figure 5). Zhang et al. (2017) have determined the number of isomers for all the hydrogenation levels of C_{60}. For $N_{CH} = 2$, 4, and 6 they computed ∼30, 10^4, and 10^6 isomers, respectively. The same number of isomers occurs for the complementary, nearly complete hydrogenation levels where $N_{CH} = 60$-2, 60-4, and 60-6. Because of its high symmetry, C_{60} has only a single isomer for $N_{CH} = 1$ and 59. For C_{36}, our estimates for $N_{CH} = 1$, 2, and 3 are approximately 3, 20, and 1200. We consider lower values of N_H for C_{36} because they correspond to comparable fractional hydrogenations as for the C_{60} values. If, for Perseus, $N_{CH} = 6$ and 3 for C_{60} and C_{36}, respectively, then the null detection abundance constraint would be satisfied. We speculate that these levels of hydrogenation are possible for Perseus because it is a cold, dense MC with a very low UV flux of $\chi_{UV} \sim 0.01$ (Draine & Lazarian 1998a).

There are other isomer sources that can increase the number of isomers by approximately an additional order of magnitude. These include the ^{13}C isotope and the diversity of C_n parents for a given carrier family (e.g., the C_{60} family consists of contributions from $\sim C_{50}$ to C_{70}). Assuming an average interstellar abundance of ^{13}C of ∼0.02, relative to ^{12}C, the fractions of ^{13}C containing isomers for C_{36} and C_{60} are 0.52, and 0.70, respectively.

In addition to the abundance constraint, there is another criterion that must be satisfied in order to obtain a null detection result. The dispersion of the emission combs needs to be comparable to the spacing between the lines. The dispersion can be estimated from $f = (\nu/2B)(\delta B/B)$, where f is the relative shift of a comb expressed as a fraction of the line spacing, $2B$, where $\delta B/B$ is a characteristic fractional change in the rotational constant and ν is the detection frequency. For C_{36}, $\delta B/B \approx 0.01$ for its analogues (see Appendix D), $\nu = 25$ GHz (0.83 cm^{-1}), $B = 0.0077\ cm^{-1}$, resulting in $f = 0.54$. We expect a significant dispersion in $\delta B/B$ values due to the many different isomers; hence, the estimated value of $f = 0.54$ is consistent with the shift criterion. Similar arguments for C_{60}, and assuming $\delta B/B = 0.003$, result in $f = 0.50$. While the shifts are sufficient to blur the line spectrum, their effect on the overall profile of a carrier family is minor. They shift the peak locations by around 1% and collectively serve to slightly broaden the profile of a carrier family.

5.4.1. Possible Detection of Line Structure in Future Observations

As just discussed, the most important factor controlling the detectability of line structure is the hydrogenation level, N_{CH}. In order to definitively detect line structure requires a value of N_{CH} that results in ≪1000 isomers, for either C_{36} or C_{60}. For C_{36}, we estimated that for $N_{CH} = 1$, 2, and 3 there are approximately 3, 20, and 1200 isomers, respectively. Thus, environments that produce a hydrogenation level of $N_{CH} = 1$ or 2 may exhibit detectable line structure for C_{36} in the spectral region where the C_{36} carrier component is most intense, typically near ∼30 GHz. The same hydrogenation levels pertain for detection of C_{60} line structure, but the optimum observation frequency range is around ∼19 GHz.

Sources with higher UV fluxes, relative to Perseus, and atom densities should favor low levels of hydrogenation (Montillaud et al. 2013). An example of such a source is the nanodiamond source, MWC 297, which appears to consist of a single carrier family and possibly only a single carrier isomer, such as HC_{60}. We need a fullerene-based hydrogenation model (Section 5.3.1), in order to determine which of the AME sources may provide detectable line structure.

Line structure may also be detected within the low-frequency side of an AME spectrum. Because the rotational constants for the hydrogenated isomers are slightly offset, their lines will separate from each with increasing frequency (i.e., higher J values) and eventually fill the interval between the parent lines. However, if one targets lower-J lines, then the isomer lines will still be clustered near their parent line positions. For Perseus, the clumps for the C_{60} carrier family may be observed in a frequency interval near 10 GHz. We would expect the clusters to occupy less than 50% of the parent line spacing (i.e., $2B = 0.17$ GHz). Hence, instead of observing equally spaced lines, one would be observing equally spaced line clusters.

5.5. Abundance Estimates for the 2CF

We ascribe the abundance estimates to fullerene-based carriers. However, the abundance estimates are weakly dependent on the identities of the carriers. The estimates apply generally to any carriers with comparable rotational constants, such as PAH molecules and VSGs. The procedure for estimating the abundances is detailed in Appendix E.

The total carbon abundances for the C_{60} and C_{36} carrier families for Perseus are $b_C = 64$ and 21. Thus, the total C abundance for the fullerene-based AME carriers is $b_C = 85$ ppm. While we have associated the abundance estimates with the average size carrier size for each carrier component, the abundances represent the total abundances for all the molecules in each of the two carrier families. As discussed later in this section, these abundances are upper limit estimates, by about a factor of 10, because they are based on

lower limit estimates of the effective dipole moments for the carrier families.

There is considerable variability in the derived carbon abundances for the other sources (see Appendix E). For ρ Ophiuchi, the CA Nebula, and LDN 1622, the C_{60} carbon abundances are $b_C = 45$, 14, and 13 ppm, respectively, as compared to 63 ppm for Perseus. The variability may reflect real variability in the carbon abundances among the sources, but it may also be due to degeneracy among the model parameters and variability in the hydrogenation levels for different sources (Section 5.3). The degeneracy arises because peak intensity of AME emission is proportional to the product of several parameters, $S_p \propto N_H \chi_{ful} \mu^2 \nu_p^n$ (Appendix A), whose values are difficult to independently quantify.

The derived abundances are consistent with the value often adopted for AME modeling based on spinning dust, $b_C = 65$ ppm (Planck Collaboration 2011b). While the range of carbon abundances accounting for AME is yet to be firmly established, it clearly represents a substantial, additional contribution to the carbon inventory (Weingartner & Draine 2001a).

Our abundance analysis reveals that a large fraction of the available carbon is tied up in the AME carriers. Averaging over the four AME sources, we estimate an average total AME carrier carbon abundance of 45 ppm. This AME carrier abundance translates into 20% of the total average interstellar carbon abundance of 225 ppm (Snow & Witt 1995). In their review, Snow & Witt (1995) show that various studies constrain the fractional abundance of carbon dust to the range of 10%–100%. Thus, the AME carrier carbon abundance is physically plausible, but it also implies that it is a substantial (up to ~40% based on Perseus AME) component of the total carbonaceous dust budget.

The above abundance estimates apply specifically to partially hyrdrogenated fulleranes, as these have dipole moments and can produce AME, as opposed to the nonpolar fullerenes. Thus, the total carbon locked up in fullerene-based molecules may be larger than the abundance estimates. From the previous discussion of nondetection of line structure in the Perseus AME, we estimated that $6 \leqslant N_{CH} \leqslant 15$ (or equivalently $15 \leqslant N_{CH} \leqslant 54$) for the C_{60} family. This implies that the abundance for the C_{60} family is approximately a factor of $1/15$ to $1/6$ (Figure 7) of its value assuming a single C–H dipole moment, as was assumed for the abundance estimate. Assuming a ballpark factor of $1/10$, then the "corrected" C_{60} abundance for Perseus is $b_C \sim 6$ ppm. Similar arguments lower the C_{36} abundance to $b_C \sim 3$ ppm, implying a total AME-based C abundance of $b_C \sim 9$ ppm. As evident in the preceding discussion, the total C abundance is sensitive to the assumed value of the effective dipole moment and likely lies somewhere in the range of $b_C \sim 9$–90 ppm.

The observationally determined interstellar abundance for the buckyball form of C_{60} (i.e., no attached H atoms) is in the range of $b_C \sim 0.02$–0.2 ppm (Cami et al. 2018). Our abundance estimate of 6 ppm for the C_{60} family includes all of its isomeric forms. If we assume of order 10^2 comparably populated isomers for the C_{60} family (Section 5.3), then we estimate a buckyball abundance in the range of $b_C = 0.06$–0.6 ppm, which is consistent with the observational range. The hydrogenation level for C_{60} corresponding to 10^2 isomers is in the range of $2 \leqslant N_{CH} \leqslant 3$. This is a plausible, low level of hydrogenation, but whether or not it is appropriate for the environments in which C_{60} has been detected awaits the development of a fullerene hydrogenation model.

5.6. C_{60}-based Carriers for the "Nanodiamond" PPD AME Sources

The possibility that nanodiamonds are the carriers of the PPD AME spectra, and possibly other AME sources, is interesting to consider (Greaves et al. 2018). Our spectral analysis of the PPD spectra shows that each spectrum is consistent with a single carrier profile. Greaves et al. (2018) also demonstrated the viability of a single carrier fit for each spectrum. This is a remarkable result, given the complex range of environments in a PPD. However, we differ from Greaves et al. (2018) in that we ascribe the PPD spectra, as well as those from all other AME sources, to fullerene-based carriers. We argue that a single fullerene parent, C_{60}, is the common carrier for the PPD AME spectra.

The three reported spectra are dissimilar and display a large spread in their peak emission frequencies, corresponding to a factor of ~5.8 between the highest and lowest T_{rot} values (i.e., MWC 297 HD 97048). PPDs encompass varied environments, and it is not known how the AME emissions are distributed within or around the disks. The PPD dust emission model developed by Greaves et al. (2018) implies that the AME could arise from a hot environment with $T_{rot} \sim 1000$ K containing relatively large particle radii, $r_p \sim 1$ nm, that are characteristic of nanodiamonds found in meteorites. However, they did not rule out much colder temperatures and smaller particles or molecules (i.e., the BT_{rot} ambiguity), as would be more consistent with the other AME sources.

It is important to realize that our identification of C_{60} and C_{36} fullerenes as the AME parent carriers is based on resolving the BT_{rot} ambiguity, which was enabled by the observation of AME for the LDN 1622 DC. A PPD source is more structurally complex and inhomogeneous than a DC source, and therefore it is more challenging to determine T_{rot}. Hence, the size and identity of the PPD carrier(s) are not well constrained.

PPD sources exhibit very intense UV radiation fields, which should result in photodestruction of all but the resilient C_{60}-based carriers. For example, MWC 297 is a Herbig Ae/Be star with an estimated UV flux at a distance of 1 au of $\chi_{UV} \sim 10^9$ (Agúndez et al. 2018). Assuming a representative disk radius of 300 au (Williams & Cieza 2011), the UV flux at this distance is $\chi_{UV} \sim 10^5$. From our earlier lifetime estimates (Section 5.2), only C_{60} should survive long enough in this environment, ~6 Myr, to be observable as an AME carrier. Even C_{60} will be destroyed relatively quickly at shorter distances from the central star. For instance, at a distance of 100 au, the C_{60} lifetime is reduced to ~0.7 Myr. C_{60}-based carriers for the PPD AME sources satisfy two challenging requirements: (1) a single carrier component spectrum, and (2) a long lifetime in an extremely intense UV radiation field.

It is unclear whether nanodiamonds can satisfy the aforementioned challenging requirements. A recent experimental and theoretical study (Candian et al. 2018a) determined that adamantane ($C_{10}H_{16}$), the smallest nanodiamond, is less stable to photodestruction than PAH molecules. However, the photostability of larger molecular nanodiamonds is an open issue.

5.7. Fullerene-based Carriers for the DIBs and UIR Bands

The interstellar molecular inventory and abundances implied by the 2FC AME model should manifest themselves in all forms of interstellar spectral observations, including the DIBs (Herbig 1995; Cami & Cox 2014) and the UIR bands (Tielens 2008; Peeters 2011). We explore the viability of the fullerene-based AME carriers as the carriers of the DIBs and UIR bands.

5.7.1. DIBs

The idea that fullerenes and fulleranes may be DIB carriers is not new (Herbig 1995). In more recent work, Bernstein et al. (2018) found that a small fullerane and PAH, with ∼30 or fewer C atoms, were plausible common carriers for the 6614 and 6196 Å DIBs. Currently, there are nearly 500 known DIBs (Cox et al. 2017). When one considers the combinatorial effect of AME carrier variations, it is not difficult to arrive at hundreds of DIBs. As discussed in Section 5.5, carrier variations include (1) different numbers of attached H atoms at different positions, (2) multiple carrier sizes for each carrier family (e.g., C_{50}–C_{70} for the C_{60} family), (3) multiple isotopologues for each carrier, and (4) cations of all the aforementioned species. There are likely orders of magnitude more potential DIBs than have been observed. The strength of a DIB is proportional to the product of the abundance of its carrier and the oscillator strength of its specific electronic transition. Both of these parameters can vary by many orders of magnitude, such that only a fraction of the potential DIBs may be observable. An AME spectrum consists of a superposition of all the above variations, whereas a DIB comprises a single, distinct band. Thus, while many AME carriers may exhibit comparable emission intensities, only a small fraction of these carriers may have sufficiently large oscillator strengths to be observable as a DIB.

Each carrier variant can produce a distinct DIB, with a unique band origin. Because the majority of DIBs are spectrally narrow, $\sim 0.7\ \mathrm{cm}^{-1}$ half-width (Webster 1996; Walker et al. 2001; Galazutdinov et al. 2008: Bernstein et al. 2015, 2018), only a small shift in the band origin is needed to produce a distinct DIB. Of all the denoted variants, isotopic substitution of a ^{13}C for a ^{12}C in a carrier produces the smallest shifts of the band origins. Nevertheless, even isotopic substitution can produce distinct DIBs (Bernstein et al. 2018). While all the carrier variants can produce distinct DIBs, they only have a minor impact on the carrier rotational constants, resulting in a slight broadening of the AME profiles for each family (Section 5.3).

The total abundance of carbon locked up in the DIB carriers is not well determined. The abundance of a DIB carrier is inversely proportional to its oscillator strength. The oscillator strength can vary by orders of magnitude and is specific for each DIB. Since the identities of virtually all the DIB carriers are unknown, save those few associated with C_{60}^+ (Campbell et al. 2015; Walker et al. 2015), it is not possible to specify their oscillator strengths. Nevertheless, we present an estimate, albeit highly uncertain, of the total C abundance in DIBs by scaling the observation-based estimate for the C abundance for C_{60}^+ of 0.2 ppm (Walker et al. 2015; Jones 2016). Assuming that all ∼500 DIBs have the same C abundance as for C_{60}^+, their total C abundance sums to $500 \times 0.2 = 100$ ppm. This C abundance is in reasonable accord with the derived AME abundance range of ∼9–90 ppm, suggesting that the DIBs and AME could originate from a common pool of carriers. They need not share exactly the same carriers, because the DIB transitions do not require a dipole moment, nor do the AME bands require an allowed electronic transition.

5.7.2. UIR Bands

The identities of the carriers of the UIR emission bands remain under discussion (Tielens 2008; Peeters 2011; Candian et al. 2018b). While PAH molecules are most often cited as the UIR carrier, none have been definitively identified. The only identified UIR carriers are the fullerenes C_{60} and C_{70} (Cami et al. 2010, 2011; García-Hernández et al. 2010; Sellgren et al. 2010; Roberts et al. 2012; Berné et al. 2013, 2017; Castellanos et al. 2014). A more tentative identification is the fullerene C_{24} as the carrier of the 11.2 and 12.7 μm bands (Bernstein et al. 2017). Zhang et al. (2017) argue that C_{60}-based fulleranes may contribute to many of the UIR features. Regardless of the specific identities of the UIR carriers, there is general agreement on several properties of the carriers, including their total C abundance and their sizes. Various estimates of the total C abundance for the carriers range from $b_C = \sim 14$ to 60 (Li & Draine 2001; Draine & Li 2007; Tielens 2008). The abundance estimates include comparable contributions from the UIR bands and underlying plateau features. Our abundance estimate for fullerene-based AME carriers ranges over $b_C = \sim 9$–90 ppm, based on analysis of the Perseus AME spectrum. As we found for the DIBs, the UIR and AME abundance estimates are comparable and consistent with the notion of a shared pool of carriers. However, AME and the UIR bands need not share exactly the same carriers, because AME requires dipolar carriers, whereas the UIR bands can arise from polar and nonpolar carriers.

Several recent spectral modeling studies of the UIR bands support the hypothesis that they may arise from a relatively small number of highly symmetric PAH molecules. One study demonstrated that ∼25, or fewer, highly symmetric compact PAH molecules can plausibly fit the UIR spectra from bright PDR regions in several reflection nebula. This idea was dubbed the "grandPAH" hypothesis (Andrews et al. 2015). The majority of grandPAH molecules are relatively small: ∼68% were found to fall in the size range of $20 < N_C < 50$, with 25% for $N_C < 30$. The size range for the proposed PAH UIR carriers overlaps well with the $N_C = \sim 30$–70 range inferred for the proposed fullerene-based AME carriers. Hence, both PAH and fullerene-based molecules may contribute to the UIR bands and AME.

While fullerene-based carriers may be significant UIR carriers, they cannot explain all the UIR bands. As discussed earlier, the C–H bond strength for fulleranes is substantially less than that for PAH molecules. As a result, the C–H(s) fundamental for fulleranes lies at or below 3.4 μm and therefore cannot account for the 3.3 μm UIR band. However, there is a 3.4 μm UIR feature that must contain a contribution from fulleranes, if they are present (Zhang et al. 2017).

The UIR bands generally refer to the relatively narrow spectral features that overlay broader plateau features and even broader continuum features (Tielens 2008). The plateau and continuum features are attributed to VSGs consisting of $N_C \sim 400$ or more C atoms that may be composed of PAH clusters and/or amorphous carbonaceous grains (Rapacioli et al. 2005; Joblin et al. 2009: Pilleri et al. 2012; Montillaud & Joblin 2014; Xie et al. 2018).

The VSGs are much larger than C_{60} and would produce AME features peaking at much lower frequencies, around 3 GHz. There are no discernible AME features in this spectral region. However, this is expected owing primarily to the power-law dependence of the AME intensity on peak frequency (i.e., ν_p^n in Appendix A). As a consequence, the AME intensities for the VSGs would be a factor of $\sim 10^{-3}$ below that for the C_{60} feature, assuming comparable dipole moments and abundances.

The fullerene-based carrier hypothesis for AME offers a potential explanation for the observed lack of positive correlation between the fluctuations of the AME and UIR band emissions (Hensley et al. 2016). The correlation study was based on the intensity of the 30 GHz AME peak as a proxy for the PAH AME abundance, and the intensity of the 11.2 μm band served as a proxy for the UIR PAH abundance. In the fullerane-based carrier model, the 30 GHz peak is composed mainly of the C_{60} and C_{36} carrier families, and the 11.2 μm band may contain a significant contribution from the C_{24} fullerene (i.e., fully dehydrogenated). There are several reasons why the C_{36}–C_{60} and C_{24} carriers may be uncorrelated. The spectral contributions of these carriers will be sensitive, in different ways, to their hydrogenation levels, which should vary strongly with the different environments hosting the UIR and AME spectra. Because of its small size, we expect that the abundance of C_{24} will vary strongly with the environment-dependent UV intensity, whereas the abundances of the C_{36}- and C_{60}-based carriers should be quite insensitive to the UV intensity.

In summary, fullerenes and fulleranes can be significant, but not exclusive, contributors to the UIR bands and DIBs, in comparable abundances and sizes as found for AME.

5.8. Relationship to Prior Spinning Dust Modeling

Spinning dust models for AME are at a mature stage of development (see review by Dickinson et al. 2018). While the models have been developed from the perspective that VSGs are the AME carriers, the distinction between VSG and molecular carriers of comparable size is largely semantics. Most dust models are framed around a classical expression for the electric dipole emission from a rotating grain. The classical approximation is comparably accurate to the more rigorous quantum mechanical approach, because the spacing of carrier rotational energy levels is small relative to thermal energies (Draine & Lazarian 1998a). We based our AME model on the symmetric top QM model of Ysard & Verstraete (2010), which can be recast in terms of a simple and accurate two-parameter (i.e., S_p and ν_p) analytic function.

The prior AME classical and quantum spectral models employ a fixed grain or molecule size distribution coupled with an assumed fixed distribution of dipole moment magnitudes. The carrier size and dipole moment distributions have been tuned to yield modeled spectra that resemble observed AME spectra for many different source environments. The distributions are constrained to be consistent with the PAH size distributions (i.e., a molecular realization of VSG's) associated with the UIR bands and dipole moments for real molecules (Draine & Lazarian 1998a).

In contrast, we consider a small number of effective carrier sizes (i.e., the parent carrier size) when fitting an AME spectrum. The spectral profile for each carrier family depends primarily on two parameters, ν_p and S_p. We have found that two distinct carrier components with relatively narrow size and temperature distributions (see Section 4.1), as opposed to a continuous distribution of carrier sizes, can accurately model AME spectra from many diverse sources. As noted earlier, the dust models have difficulty fitting some of the finer details of an AME spectrum (see Perseus SPDUST.2 fit in Figure 5), which we attribute to the assumed continuous carrier size distribution.

5.8.1. Polarization of Fullerene-based Carriers

The fullerene-based AME carriers are consistent with the small upper limits determined for the polarization of AME. The AME polarization measurements are highly variable, with a median upper limit value of a ~2% polarization fraction in the 20–40 GHz region, where AME typically peaks (Dickinson et al. 2018). Theoretical predictions by Draine & Hensley (2016) demonstrated that the alignment of very small grains or molecules, in the size range considered here, by a magnetic field is suppressed owing to quantum effects. Their estimates of the polarization fraction for these carriers, which encompasses ferromagnetic carriers such as a fullerene with a caged Fe atom, fall orders of magnitude below the experimental upper limit of a ~2% polarization fraction.

5.9. Timescale for Fullerene Accretion onto Grains in a Dark Cloud

The fullerene-based carrier hypothesis requires that a significant fraction of the carriers in a cold dense DC remain in the gas phase, in order to produce a measurable AME signal. In Appendix F, we present the mathematical details for estimating the timescale for fullerene accretion onto grains. We consider both carbonaceous and siliceous grains and base the estimate on the Mathis, Rumpl, & Nordsieck (MRN) grain size distribution (Mathis et al. 1977). For a typical DC condition, $T_K = 10$ K, $n_{\rm H} = 1 \times 10^4\,{\rm cm}^{-3}$, we estimate an accretion timescale of 2 Myr for the C_{60} carrier analogues. This is a lower limit estimate because it is based on a sticking coefficient of unity. For comparison, we adopt an upper limit to the lifetime of a DC of ~6 Myr (Pagani et al. 2011), but note that there is considerable uncertainty with regard to the estimation of MC lifetimes (Heyer & Dame 2015). Assuming an average DC lifetime of 3 Myr, the accretion fraction for the C_{60} carrier family will be $1 - e^{-3/2} = 0.78$. Doubling the DC lifetime or halving the accretion timescale increases the fractional accretion to 0.96 (i.e., only 4% of the AME carriers left in the gas phase), suggesting that many DC and cold core AME signals may be too weak to detect. Nonetheless, a higher-density DC or cold core should be detectable, if caught early in its lifespan, before accretion has progressed too far. Hence, the fractional accretion can vary considerably, depending on the actual age and $n_{\rm H}$ density (scaling factor for dust density) of a specific DC of interest.

We found that the abundance estimate for the C_{60} carrier family for the LDN 1622 DC was the lowest of the sources considered (Appendix E). The C_{60} abundance estimates are $b_{\rm c} = 63$, 11, 48, and 11 ppm for Perseus, LDN 1622, ρ Ophiuchi, and the CA Nebula, respectively. Part or all of the variability in $b_{\rm c}$ could also arise from environment-dependent variations in the hydrogenation level, which affects the AME intensity (Section 5.3).

The accretion timescales for the other carrier families will be comparable to that for C_{60} because the collision cross depends primarily on the grain size. There is a modest correction due to the mass dependence of the carrier collision velocity (i.e., $v \propto 1/m^{1/2}$).

5.9.1. UV Photodesorption

We consider the impact of UV photodesorption of an adsorbed fullerene on the accretion process. There is a weak van der Waals attraction between an adsorbed fullerene and the grain surface, which renders it susceptible to UV photodissociation. For example, the bond energy of C_{60} on graphite is ~0.85 eV (Ulbricht et al. 2003), which is much less than the energy for a typical chemical bond, 4 eV, or an absorbed UV photon, ~10 eV.

The key consideration is how quickly the absorbed UV energy, initially localized within the fullerene, redistributes throughout the grain. The redistribution timescale is not known. If it is "slow," then the vibrationally excited fullerene can desorb. The desorption proceeds along a fullerene-surface vibrational coordinate corresponding to breaking of the van der Waals bond.

If a significant fraction of the absorbed UV photons result in a fullerene desorption, then the rate of accretion will be significantly diminished. The timescale for absorption of a UV photon is $\sim 10^7/\chi_{\rm UV}$ s. For a DC environment, $\chi_{\rm UV} = 10^{-4}$, the UV absorption timescale is 10^{12} s or 0.003 Myr. The photoabsorption timescale is much smaller than the accretion timescale of 2 Myr. If each absorbed UV photon produces a desorbed fullerene, the steady-state fractional accretion would be small, 0.003 Myr/2 Myr = 0.0015. Even if the efficiency of the photodesorption process is as low as 1% per absorbed UV photon, the fractional accretion would still be appreciably below unity, ~0.15. Hence, UV photodesorption may substantially impact the accretion process. Molecular dynamics simulation of the energy redistribution and photodissociation processes could quantify the photodesorption timescale.

5.10. Recommendations for Future Investigations

We consider improvements to the spectral model and future AME observations that will enable a more refined evaluation of the 2CF hypothesis for AME. We also consider the potential contributions of fullerenes and fulleranes to the DIBs and UIR bands.

1. *An improved fullerene-specific collisional excitation/relaxation model*: Enables a more accurate determination of $T_{\rm rot}$ (given T_K and $n_{\rm H}$) for more environments, MC in particular, and results in an independent retrieval of B for more environments. The envisioned improvements would include collision-partner-specific, multidimensional interaction potentials and state-to-state excitation and relaxation cross sections.
2. *Fullerene-based hydrogenation model*: Enables prediction of AME intensity variations for different environments. Also needed for prediction of the effective dipole moment for use in the collisional model determination 7of $T_{\rm rot}$.
3. *Improved signal-to-noise ratio and spectral sampling above ~50 GHz for observation of a few AME sources (e.g., Perseus and LDN 1622)*: Enables better separation of AME from the other background components and addresses the existence (or not) of the third C_{20} carrier family.
4. *Computational chemistry modeling of the fullerene and fullerane IR cascade spectra*: Build on the work of Zhang et al. (2017) and Adjizian et al. (2016) to evaluate the potential contribution of fullerenes and fulleranes to the UIR bands and plateau features. The calculations should incorporate recent improvements to modeling the effects of anharmonicity (Mackie et al. 2018).
5. *Perform laboratory measurements of fullerene and fullerane near-IR–UV emission and/or absorption spectra*: Look for matches with the known DIB spectra. Theoretical predictions do not produce sufficiently accurate band origins for identification purposes.
6. *Improve the observational spectral sampling for the Gould Belt and NGC 4725 AME spectra*: Provides a partial validation test of the 2CF model, as significant spectral structure was predicted that is currently absent in the model comparisons to the sparsely sampled data.
7. *Perform high spectral resolution AME measu*rements: Look at sources with low levels of hydrogenation, $N_{\rm CH} \leqslant 2$, to reduce the number of fullerane isomers and thereby increase the probability of seeing line structure. This should favor sources with high UV fluxes and low H atom densities. Finally, look at a window around 10 GHz, where resolved spectral clumps may be observed.

6. Summary

We determined that two carrier families, clustered around distinct carrier sizes, could credibly model AME spectra from 14 diverse galactic and extragalactic sources. This finding is irrespective of the carrier type, fullerane, PAH molecules, or VSG and rests primarily on the assumption of a symmetric top carrier.

We introduced a 2CF spectral model composed of four adjustable parameters, a peak height and peak frequency for each of the two carrier families. The 2CF fits revealed that the ratios of the peak heights and peak frequencies for most of the spectra were approximately constant, varying in unison for diverse source environments. Using a Monte Carlo hydrogenation simulation model, we demonstrated that fullerene-based carriers could exhibit in-unison variability.

The sizes of the two parent carriers are reasonably well established. This followed because the rotational temperatures for the carriers in a DC source, LDN 1622, are well determined. For high-density sources, such as a DC, $T_{\rm rot} = T_K$, which enables resolution of the $BT_{\rm rot}$ ambiguity. The derived parent carrier sizes correspond closely to the C_{36} and C_{60} fullerenes. Each carrier family consists of a range of carrier sizes centered on the parent carrier. For example, the C_{60} family encompasses the C_{50} to C_{70} fullerenes.

By virtue of their exceptional stability to UV photodissociation, fulleranes are likely to be significant, perhaps dominant, AME carriers. Based on the extraordinary stability of C_{60}, we hypothesized that it may be the only AME parent carrier that can survive the harsh UV environment of the PPD nanodiamond AME sources, thereby offering an explanation for the observation of single carriers for these sources.

The substantial derived C abundances for the AME carriers, ~4%–40% of the total C, should have observable

consequences in other spectral regions, in particular, those corresponding to the DIB absorption and the UIR emission bands. The large number of fullerane isomers is consistent with the current catalog of some 500 DIBs. Laboratory measurements are required to find DIB matches, as theoretical methods cannot predict the band locations with sufficient accuracy. We recommend computational chemistry modeling of the fullerene and fullerane IR emission bands for comparison to observed UIR bands and plateaus.

Finally, the most definitive identification of an AME carrier would be through the observation of line structure in an AME spectrum. We predicted that line structure may be observable for high UV flux and low-density H atom AME sources that produce hydrogenation levels of $N_{CH} \leqslant 2$ for either the C_{36} or C_{60} carrier families.

L.S.B., R.M.S., and J.Q. appreciate funding for this project from Spectral Sciences, Inc., and L.S.B. appreciates additional support from Maine Molecular Sciences. C.D. acknowledges support from an STFC Consolidated Grant (ST/P000649/1). We thank M. Braunstein (Spectral Sciences, Inc.) and G. Radhakrishnan (The Aerospace Corp.) for technical discussion. We appreciate the insights and suggested revisions provided by the anonymous reviewers, which have substantially improved the paper.

Appendix A
Derivation of the Analytic AME Spectral Model

We derive the analytic function used for fitting the observed AME spectra, which applies to spherical top fullerane carriers, and discuss modification of the fitting function for symmetric top compact PAH carriers. The analytic spectral profile model is based on the QM modeled used by Ysard & Verstraete (2010), which is given by

$$S_J(\mathrm{Jy}) = 10^{23}\chi_{\mathrm{ful}}N_{\mathrm{H}}(\mathrm{cm}^{-2})A_{J,J-1}(\mathrm{s}^{-1})P_J \times \frac{h\nu_J(\mathrm{erg})}{2B(\mathrm{Hz})}\frac{\Omega(\mathrm{sr})}{4\pi}, \quad (8)$$

where the constant 10^{23} is the conversion factor between cgs units and Jy, χ_{ful} is the carrier mole fraction, N_{H} is H atom column density, $A_{J,J-1}$ is the Einstein A-coefficient for the $J \rightarrow J-1$ transition, P_J is the population of the Jth rotational state, $h\nu_J$ is photon energy, and Ω is the detection beam angular extent. For a symmetric top, the Einstein A-coefficient and the rotational state population depend on the rotational quantum number K (Ysard & Verstraete 2010). However, the emission energy does not depend on K, because the rotational emission selection rules are $\Delta J = -1$ and $\Delta K = 0$. For simplicity, the form for the symmetric top emission in Equation (7) presumes that the Einstein A and state population factors have been averaged over their K dependences, resulting in factors that depend only on J.

The Einstein A-coefficient for a symmetric top molecule and for $J \gg 1$ is computed from (Ysard & Verstraete 2010)

$$A_{J,J-1} = 2.67 \times 10^{-11}J^3\left(\frac{B}{B_0}\right)^3\left(\frac{\mu}{\mu_0}\right)^2, \quad (9)$$

where $B_0 = 0.02\,\mathrm{cm}^{-1}$ and $\mu_0 = 2$ D. The rotational state population is calculated using

$$P_J = 0.973\left(\frac{B}{T_{\mathrm{rot}}}\right)^{3/2}(2J+1)^2\exp\left(-\frac{c_2BJ(J+1)}{T_{\mathrm{rot}}}\right), \quad (10)$$

where B is in units of cm^{-1} and $c_2 = 1.4387\,\mathrm{K\ cm}$. This expression is based on a spherical top molecule and includes a degeneracy factor of $2J+1$ for the spectrally degenerate K states.

The continuous analytic form used in the spectral fitting (see Equation (1)) follows from the substitution of $\nu = 2BJ$ into Equation (8), which leads to

$$S_\upsilon = a_0\upsilon^6\exp\left(-\left\{\frac{\upsilon}{\upsilon_0}\right\}^2\right), \quad (11)$$

where a_0 is a normalization constant and ν_0 is defined by

$$\upsilon_0^2 = \frac{4BT_{\mathrm{rot}}}{c_2}. \quad (12)$$

We can reexpress and generalize Equation (11) in terms of the frequency at the peak emission intensity, ν_p, which results in Equation (1),

$$S(\upsilon) = S_pa_n\left\{\frac{\upsilon}{\upsilon_p}\right\}^n\exp\left(-\frac{n}{2}\left\{\frac{\upsilon}{\upsilon_p}\right\}^2\right), \quad (13)$$

where ν_p is related to molecular constants through

$$\upsilon_p = \sqrt{\frac{2n}{c_2}BT_{\mathrm{rot}}}. \quad (14)$$

The generalized form for S_ν in Equation (13) applies to symmetric top, $n = 6$, and linear molecules, $n = 5$, and also allows for incorporation of empirically derived broadening effects and different angular momentum distributions (see Appendix C).

The rotational quantum number and the emission frequency at the peak emission for a symmetric top are related by

$$J_p = \frac{\upsilon_p(\mathrm{cm}^{-1})}{2B(\mathrm{cm}^{-1})}. \quad (15)$$

For this study, $n = 5$ (see Appendix C); however, other values of n are possible for different carrier geometries and different assumptions with regard to the distribution function for J (Ali-Haïmoud et al. 2009; Ysard & Verstraete 2010).

The expressions above pertain explicitly to a spherical top (i.e., $A = B = C$), motivated by our focus on fullerane carriers. The effects of considering a symmetric top, such as a compact PAH with $A = B = 2C$, would have minimal impact on the results of this study. The two carrier component fits would be unaffected, that is, the same S_ν and ν_p parameter values would apply. The most significant difference relates to the relationship between B and T_{rot}. For a compact PAH, the BT_{rot} fitting constraint would be reduced by a factor of 0.864 relative to a spherical top. For example, if one assumes a temperature of $T_{\mathrm{rot}} = 18.5\,\mathrm{K}$ for Perseus, then $B = 0.0024$ versus $0.0028\,\mathrm{cm}^{-1}$ for a spherical top. This PAH rotational constant translates into $N_{\mathrm{C}} = 52$ versus 60 for a spherical top.

Appendix B
Spectral Fitting Methodology

In the first fitting step, the model parameters were initialized by shifting the two-profile Perseus fit to match the spectrum under consideration. This was accomplished using a single multiplicative parameter applied to the emission frequency scale, $\nu' = \beta\nu$, where ν refers to the Perseus model spectrum. In the second step, the shifted spectrum was also adjusted to best match the spectrum under consideration. In the third and final step, the peak heights and peak frequencies of the two profiles were independently varied. The resulting fit parameters are presented in Table 1, and a detailed discussion of the method is presented below.

Measured data were fit by the method of least squares to an analytical function using the L-BFGS-B minimization algorithm (Byrd et al. 1995; Virtanen et al. 2020) as implemented by SciPy (Zhu et al. 1997). Prior to analysis, the observed AME spectrum, $S(\nu_k)$, was divided by their trapezoid integral, C,

$$C = \sum_k \frac{S(\upsilon_{k-1}) + S(\upsilon_k)}{2}\Delta\upsilon_k, \tag{16}$$

where $\Delta(\nu_k)$ is the spacing between points and the normalized spectrum is $S' = S/C$. The fitting function for the discretely sampled observational spectral sequence $f(\nu_k)$ is given by

$$f(\upsilon_k; A_i, B_i) = \sum_{i=1}^{N} A_i \left(\frac{\upsilon_k}{B_i}\right)^n \exp\left(-\frac{n}{2}\left(\frac{\upsilon_k}{B_i}\right)^2\right), \tag{17}$$

where i is the profile index and N is the number of fitting profiles $\{N|1 \text{ to } 4\}$. The summed squared error, χ^2, is

$$\chi^2 = \sum_k \frac{[f(\upsilon_k) - S'(\upsilon_k)]^2}{\delta(\upsilon_k)^2}, \tag{18}$$

where $\delta(\nu_k)$ is the normalized error reported for the measured data, $S'(\nu_k)$. The data fitting minimized χ^2 via the optimization of the parameters A_i and B_i. Parametric dependence, indicated by the semicolon, is used to denote optimization parameters. Note that for Figure 5 we used the reduced χ^2, which is given by Equation (18), divided by the number of degrees of freedom. The number of degrees of freedom is defined as the number of data points minus the number of adjustable parameters.

Fitting was first applied to the Perseus data over a range of n and N values, $\{n \,|4 \text{ to } 6\}$ and $\{N \,|1 \text{ to } 4\}$, respectively (see Figure 5). Each fitting was performed for a fixed (n, N) pair. To reduce the likelihood of finding a local minimum, 100 optimizations were performed for each fitting, with different initial parameters selected at random from a range of values. An F-test analysis was performed on the final results, and $(n, N) = (5, 2)$ was selected based on physics-based arguments and statistical significance for further application to most observed AME spectra.

The AME spectra in Figure 1 were fit using a multistep optimization procedure after data normalization. The procedure was developed to provide a consistent robust fitting for all spectra, including those with very few data points and features consistent with overfitting. The peak locations from the two-profile Perseus fit were used to fit AME spectra with a single parameter, β. The first step was performed using

$$\begin{aligned} f_{\text{Step1}}(\upsilon_k; \beta) \;=\; & A_0^P \left(\frac{\upsilon_k}{\beta B_0^P}\right)^n \exp\left[-\frac{n}{2}\left(\frac{\upsilon_k}{\beta B_0^P}\right)^2\right] \\ & + A_1^P \left(\frac{\upsilon_k}{\beta B_1^P}\right)^n \exp\left[-\frac{n}{2}\left(\frac{\upsilon_k}{\beta B_1^P}\right)^2\right], \end{aligned} \tag{19}$$

where the superscript p denotes the Perseus fit value. A total of 100 optimizations were performed for each AME spectrum starting with random values of β. The value of β yielding the minimum χ^2 was retained and used to initialize subsequent steps. The second step optimized the profile heights while keeping the profile peaks fixed at constant β,

$$\begin{aligned} f_{\text{Step 2}}(\upsilon_k; A_0, A_1) = & A_0 \left(\frac{\upsilon_k}{\beta B_0^P}\right)^n \exp\left[-\frac{n}{2}\left(\frac{\upsilon_k}{\beta B_0^P}\right)^2\right] \\ & + A_1 \left(\frac{\upsilon_k}{\beta B_1^P}\right)^n \exp\left[-\frac{n}{2}\left(\frac{\upsilon_k}{\beta B_1^P}\right)^2\right]. \end{aligned} \tag{20}$$

The values of A_0 and A_1 yielding the minimum χ^2 were retained and used to initialize the final step. The first two steps provided the initial inputs for the third and final full optimization using the full optimization function,

$$f_{\text{Step3}} = f(\upsilon_k; A_i, B_i). \tag{21}$$

The parameters yielding the minimum χ^2 were retained and reported.

The fitting procedures for the "special cases" (i.e., very sparse sampling and multiple sources) of observed AME spectra in Figures 2 and 3 are based on straightforward variations to the methodology presented above. The variations are discussed in the main text (Sections 3.4 and 3.5).

Appendix C
Angular Momentum Distributions

We consider the effect of different assumed angular momentum distributions on the 2CF model fits to AME spectra. The angular momentum distribution depends on a variety of environment and intrinsic molecular properties, many of which are not known for specific AME sources (Ali-Haïmoud et al. 2009; Ysard & Verstraete 2010). In order to assess the sensitivity of the 2CF spectral fits to variations in the angular momentum distribution, we assume that the angular momentum distribution functions can be parameterized as

$$P_J \propto J^m \exp\left(-\frac{c_2 B J(J+1)}{T_{\text{rot}}}\right), \tag{22}$$

where $m = 2$ corresponds to the Maxwellian distribution for a symmetric top molecule (see Appendix A). In this work, m is treated as an empirical parameter and used to test the sensitivity of the resulting fit to the angular momentum distribution. The left panel of Figure 8 shows examples of P_J for different values of m. As is evident, the distributions are very different. However, as displayed in the right panel of Figure 8, the corresponding differences in the fits to the observed Perseus spectrum are relatively modest. The uncertainties in the angular momentum distributions do not impact either the key result of

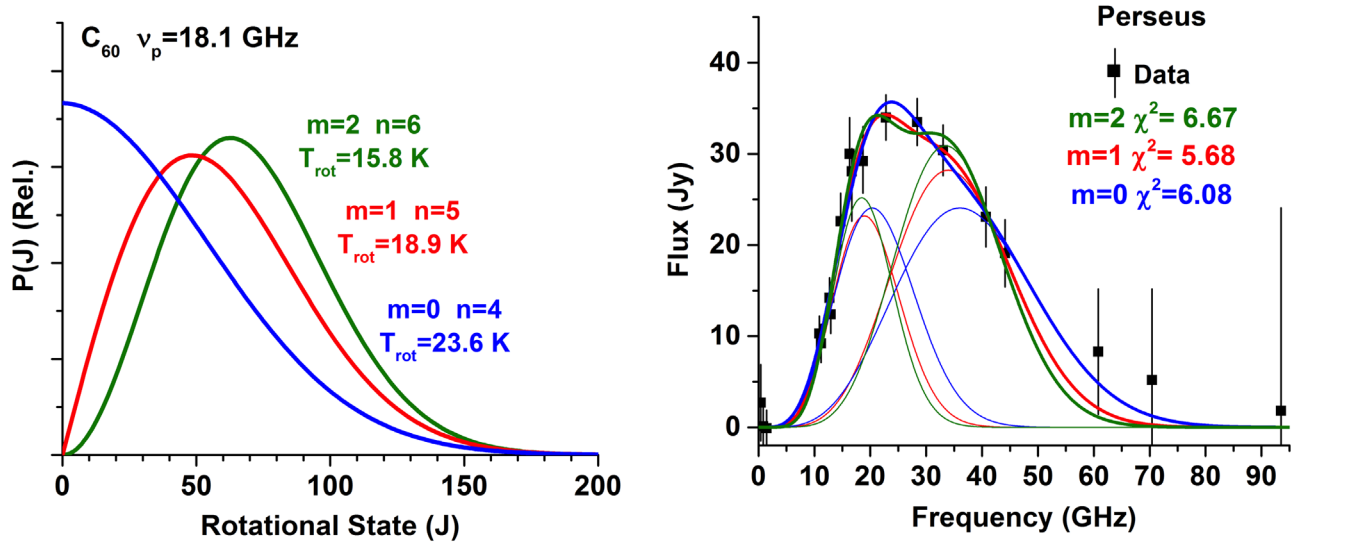

Figure 8. Sensitivity of the spectral model fit to the observed Perseus AME spectrum (black squares with vertical lines for the uncertainties) for different representations of the angular momentum distribution function. We consider three representations of the angular momentum distributions defined by Equation (15) for $m = 2$, 1, and 0, which correspond to $n = 6$, 5, and 4 for the exponent of the $(\nu/\nu_p)^n$ factor in the analytic model (see Equation (1)). Examples of the three angular momentum distributions are shown in the left panel for the 18.1 GHz fit component based on a C_{60} analog carrier. The distributions are normalized to the same integrated area. The value of $T_{\rm rot}$ for each distribution was varied in order to maintain the same fit peak location (see Equation (3)). The right panel depicts the model fits (thick colored curves) to the observed Perseus spectrum for the three angular momentum distributions. The two molecular components for each fit are also shown (thin colored curves).

the study (i.e., two carrier families) or the viability of C_{36} and C_{60} as the parent carriers.

The main effects of changing the angular momentum distribution function are modest changes in the widths and heights of the three molecular components. In this study, we adopted $m = 1$, $n = 5$ because it produces a slightly better fit to the Perseus spectrum than $m = 2$ or $m = 0$. We interpret the results as those of a symmetric top under the assumption of additional broadening. We assumed $n = 5$ for all the data fits. In reality, one expects that n will depend to some extent on many factors, such as carrier size, dipole moment, environment conditions, etc. However, the signal-to-noise ratios and spectral resolutions of the available AME data are not sufficient to allow for an empirical determination of the variability of n.

C.1. Impact of IR Radiative Cascade on the Angular Momentum Distribution

We consider the effect of the IR radiative cascade, following the absorption of a UV photon, on the angular momentum distribution. The emission of an IR photon typically changes the total angular momentum by $\Delta J = \pm 1$. For perpendicular bands, 1/3 of the transitions occur with $\Delta J = 0$ (Q-branch). The IR cascade is analogous to a quantized-step random walk process because there is a nearly equal and uncorrelated probability of $\Delta J = +1$ or -1 for each emitted photon. The emission of multiple ($n_{\rm IR}$) photons will broaden the angular momentum distribution by $|\Delta J| \sim n_{\rm IR}^{1/2}$. For the absorption of a 10 eV UV photon and an average IR photon energy of $\sim$1000 $\rm cm^{-1}$, $n = 81$, resulting in $|\Delta J| \sim 8$. For comparison, the typical rotational quantum number associated with the peak emission for the C_{60} fit component is around $J_p \sim 100$ (see Appendix E). This means that the effect of a single UV photon on the width of the angular momentum distribution is minor, roughly $|\Delta J|/J_p \sim 0.08$. The actual broadening effect is reduced by a factor of 0.25 because it adds in quadrature to the other width contributions. Thus, if the rate of absorbing a UV photon is comparable to, or less than, the rate of collisional excitation/relaxation, then the IR radiative cascade has minimal impact on the angular momentum distribution.

We expect the IR radiative cascade process to be most important for environments with low ambient densities (i.e., low collision rates) and high UV radiation fields (i.e., high UV photon absorption rates). For the four AME environments considered in Figure 5, the CNM environment comes the closest to satisfying these properties.

For the CNM environment, we estimate a collision rate of H atoms with C_{60} of $6 \times 10^{-8}\,\rm s^{-1}$ (Section 4). For comparison, the CNM environment has a UV flux of $\chi_{\rm UV} = 1$, producing a UV photon absorption rate of $\sim 2 \times 10^{-8}\,\rm s^{-1}$, based on integration over the 8–13.6 eV photon energy range, which is significantly smaller than the collision rate of $6 \times 10^{-8}\,\rm s^{-1}$. Hence, for the CNM environment the IR radiative cascade has no significant impact on the angular momentum distribution for the C_{60} carrier family. We expect that this result also holds for the C_{36} carrier family. Comparable estimates for other environments predict that the effect of the IR cascade process would be insignificant for the DC, MC, and PDR environments, whereas it would be significant for the WNM, WIM, and RN environments. As mentioned earlier, there is no compelling observational evidence that AME arises from environments, such as the WNM, WIM, and RN, with large H^+ mole fractions (Planck Collaboration 2011b; Dickinson et al. 2018). The effects of the IR cascade are accommodated in our spectral fitting model through the J^m term in Equation (22), which controls the broadening of the AME spectral profile (Figure 4).

Appendix D
Dipole Moments and Rotational Constants for Fullerene Analogues

In order to emit rotational photons, a carrier must have a permanent dipole moment, μ. The intensity of the rotational

Table 2
Summary of Results for the Fullerene C_{36}, C_{60}, and Related Compounds, where *sym.* is Point Group, m_s is Spin Multiplicity (i.e., $m_s = 1$ or 2 for None or One Unpaired Electrons), μ is the Total Dipole Moment, q is Partial Charge on Attached Fe or H Atom, E_b is Bond Energy Relative to the Separated H and Fe Atoms, E_{rel} is a Relative Energy Difference between Different Analogues (see text), and B Denotes the Three Rotational Constants

Molecule	*Sym.*	m_s	μ (D)	$q_{H/Fe}$ (e)	E_B (eV)	E_{rel} (eV)	B (10^{-3} cm^{-1})		
C_{36}	C_{2v}	1	0.22	⋯	⋯	0	8.41	7.63	7.32
$C_{36}H(i)$[a]		2	0.27	0.29	−0.21	0	8.36	7.48	7.37
$C_{36}H(e)$[a]		2	1.88	0.22	−3.57	0	8.41	7.47	7.29
$C_{36}Fe$		5	1.36	0.09	−1.32	0	8.37	7.34	7.24
C_{36}	D_{6h}	1	0.00	⋯	⋯	0.49	8.66	7.44	7.29
$C_{36}H(i)$		2	0.38	0.38	−0.64	0.07	8.65	7.32	7.27
$C_{36}H(e)$		2	1.53	0.22	−4.06	0.01	8.71	7.25	7.23
$C_{36}Fe$		5	0.32	0.15	−1.92	−0.11	8.61	7.29	7.21
C_{60}	I_h	1	0.00	⋯	⋯	⋯	2.78	2.78	2.78
$C_{60}H(e)$		2	1.48	0.06	−2.13	⋯	2.78	2.76	2.75

Note.
[a] Interior (i) or exterior (e) H atom.

emission is proportional to μ^2. The high symmetry of most fullerenes, such as the spherical top C_{60}, precludes a dipole moment; hence, they cannot emit rotational photons. There are lower symmetry fullerenes, such as a C_{2v} isomer of C_{36} described below, that can exhibit a dipole moment, but it is generally small in magnitude. However, there is a broad range of fullerene analogues with an externally (exohedral) or internally (endohedral) attached atom, such as an H and Fe atom, that can display substantial dipole moments. Uncertainty in the dipole moment results in uncertainty in identifying the exact carrier and carrier abundances. Here we calculate a range of dipole moments for a number of candidate molecules. We scratch the surface of this complicated configuration problem by taking a cursory look at some of the possible polar forms of C_{36}.

The geometry, total electronic energy, and zero-point vibrational energy for each species was computed using the hybrid range-separated dispersion-corrected density functional, ωB97X-D (Chai & Head-Gordon 2008). This functional has been found to give very good results for organometallic systems when compared with other density functionals (Minenkov et al. 2012). The 6-31G basis set was used for H atoms (Hehre et al. 1972), 6-31G* for C atoms (Hariharan & Pople 1985), and the LANL2DZ basis and effective core potential for Fe (Hay & Wadt 1985). The partial atomic charges were determined through a Mulliken population analysis (Mulliken 1955). Calculations on C_{36}, $C_{36}H$, and $C_{36}Fe$ were conducted with the GAMESS quantum chemistry software, (Schmidt et al. 1993), and calculations on C_{60} and $C_{60}H$ were conducted with Gaussian03 (Frisch et al. 2009).

The results of our quantum chemistry studies are given in Table 2. The $C_{36}H(i)/C_{36}Fe$ species is the C_{36} fullerene with a single H/Fe atom on the inside of the cage, and $C_{36}H(e)$ contains a single H atom bonded to the exterior of the cage. The symmetry label applies only to the bare fullerene. Table 2 gives the electric dipole, μ, the partial charge on the H or Fe atom, $q_{H/Fe}$, the rotational constants, B, and two zero-point-corrected energies that provide information on the relative energetic stability of each species. The binding energy, E_B, is the energy of the fullerene-H/Fe complex relative to fullerene and the H/Fe atom at infinite separation, e.g., $C_{36} + Fe \rightarrow C_{36}Fe$. The relative energy, E_{rel}, is the energy difference between the C_{2v} and the D_{6h} isomers of the C_{36} fullerene, C_{2v}–D_{6h}, for that species. See Małolepsza et al. (2007) for a description of the topological isomers of C_{36}.

Appendix E
Carrier Abundance Estimation

We estimate the abundances for the three fullerene-based carrier families. The abundance estimates are weakly dependent on the identities of the carriers. They apply generally to any carriers with comparable rotational constants, such as PAH molecules and VSGs.

The carrier abundances were estimated using the QM expression (Ysard & Verstraete 2010) to model the detected power emitted from a spectrally unresolved single line of a symmetric top molecule averaged over the spacing between lines,

$$S_J = \chi_{ful} N_H A_{J,J-1} P_J \frac{h\nu_J}{2B} \frac{\Omega}{4\pi}, \quad (23)$$

where S_J is the emitted flux from the J rotational state, χ_{ful} is carrier abundance relative to n_H, $A_{J,J-1}$ is the Einstein A coefficient for rotational emission from J, P_J is the population of the J state, $h\nu_J$ is the energy of the emitted photon at frequency ν_J, $2B$ is the spacing between emission lines, and Ω is the solid angle of the emitting source. P_J is dependent on T_{rot}, and $A_{J,J-1}$ is proportional to μ^2. The details for evaluating Equation (23), in order to solve for the carrier abundance, χ_{ful}, are presented in Appendix A, and the results are summarized in Table 3 for Perseus and several other AME sources.

The abundance estimates specifically refer to the fullerane carriers, because they are dipolar and can produce AME. Fullerenes and fully hydrogenated fulleranes do not have dipole moments and cannot produce AME. Estimation of their abundances would require a hydrogenation model in order to relate the nonpolar to the polar abundances.

Values for the quantities in Equation (23) were obtained from the preceding spectral analysis and prior estimates of the source environment parameters. The derived abundances, relative to that for H, for the C_{60} and C_{36} carrier families for Perseus are $b_C = 64$ and 21 ppm, respectively. While we have associated the abundance estimates with the average carrier size for each carrier component, the abundances represent the total abundances for all the molecules in their carrier families. The C_{60} carrier component abundance estimates for ρ Ophiuchi, CA

Table 3
Parameter Values Used in Equation (23) for Estimation of Carrier Abundances for Perseus, ρ Ophiuchi, CA Nebula, and LDN 1622

Parameter	Perseus C_{60}	Perseus C_{36}	ρ Ophiuchi C_{60}	CA Nebula C_{60}	LDN 1622 C_{60}
N_H (cm^{-2})	1.2×10^{22}	1.2×10^{22}	1.8×10^{22}	3.3×10^{21}[a]	2.4×10^{22}
Ω (sr)	6.85×10^{-4}	6.85×10^{-4}	2.47×10^{-4}	6.00×10^{-4}	1.71×10^{-4}
T_{rot} (K)	21.3	21.3	38.7	64.3	18.5
μ (D)	1.6	1.1	1.6	1.6	1.6
B (cm^{-1})	0.00277	0.0077	0.00277	0.00277	0.00277
B (Hz)	8.31×10^{7}	2.31×10^{8}	8.31×10^{7}	8.31×10^{7}	8.31×10^{7}
ν_p(GHz)[b]	19.0	34.0	25.6	33.0	17.7
ν_p (cm^{-1})	0.633	1.13	0.853	1.10	0.590
$h\nu_p$ (erg)	1.26×10^{-16}	2.24×10^{-16}	1.70×10^{-16}	2.18×10^{-16}	1.17^{-16}
J_p	114	74	152	199	107
P_{Jp}	6.51×10^{-3}	8.28×10^{-3}	5.00^{-3}	3.72×10^{-3}	6.84×10^{-3}
$A_{Jp,Jp-1}$ (s^{-1})	6.73×10^{-8}	1.87×10^{-7}	1.59×10^{-7}	3.58×10^{-7}	5.56×10^{-8}
S_p (Jy)[b]	23.0	28.8	21.8	3.7	1.9
χ_{ful}	1.06×10^{-6}	5.97×10^{-7}	1.66×10^{-7}	1.77×10^{-7}	2.17×10^{-7}
b_c (ppm)[c]	63.5	21.1	45.3	14.1	13.1

Notes.
[a] Remy et al. (2017).
[b] From two-component fit (see Table 1).
[c] $b_c = 10^6 N_C \chi_{ful}$.

Nebula, and LDN 1622 are $b_C = 45$, 11, and 13 ppm, respectively. We note that the three-profile fit for Perseus (bottom panel of Figure 5) implies a C_{20} carrier family with a C abundance of $b_C \sim 0.6$ ppm.

Appendix F
Accretion of Fullerenes onto Grains

We estimate the timescale for physisorption of fullerenes onto grains, because carriers stuck on grains do not produce AME. The estimate is based on the MRN grain size distribution (Mathis et al. 1977),

$$\frac{dn_{gr}}{dr} = \frac{2Cn_H}{r^{3.5}}, \tag{24}$$

where n_{gr} is the number density of grains with radius r, $C = 10^{-25.1}\,cm^{-3.5}$, $r_{min} = 5.0 \times 10^{-7}$ cm (i.e., 50 Å), $r_{max} = 3.0 \times 10^{-5}$ cm (i.,e., 3000 Å), and n_H is the number density of H (scaling factor for dust density). The factor of 2 in the numerator accounts for both carbonaceous and siliceous grains, for which the same value of C applies (Weingartner & Draine 1999). The total collision rate of a fullerene with the grains is given by

$$\begin{aligned} z_{col} &= vS_{gr}\int_{r_{min}}^{r_{max}} dr \frac{dn_{gr}}{dr}\pi r^2 \\ &= 3\pi vS_{gr}Cn_H[r_{min}^{-1/2} - r_{max}^{-1/2}], \end{aligned} \tag{25}$$

where v is the average velocity of the fullerene and S_{gr} is the sticking coefficient for physisorption of the fullerene onto the grain. We assume a sticking coefficient of unity, $S_{gr} = 1$, which establishes a lower limit estimate for the accretion timescale. We evaluate this expression for the typical conditions of a DC, $T_K = 10$ K, $n_H = 1 \times 10^4\,cm^{-3}$, and $v = 1.71 \times 10^3\,cm\,s^{-1}$ for C_{60}. The result is $z_{col} = 2.3 \times 10^{-14}\,s^{-1}$, which corresponds to an accretion timescale of $\tau_{acc} = 1/z_{col} = 2.0$ Myr.

The preceding analysis did not consider the effect of grain charge on the accretion rate. For a DC environment, approximately 50% of the grains, in the size range of interest, will be negatively charged, and ~90% of the molecules will be neutrally charged (Draine 2004). The primary interaction between a charged grain and a neutral polar fullerane will be via a charge–dipole interaction, $E \propto q\,\mu\cos(\theta)/r^2$, where $q = -1$ is grain charge and θ is the orientation of the dipole with respect to a line connecting the centers of mass of the collision pair. We estimate an effective interaction distance as the distance at which the interaction and the collision energies are equal, since collisions with impact parameters greater than this distance would not result in capture. We adopt several approximations in order to derive an upper limit estimate to the interaction distance, including (1) a nonrotating molecule with its dipole aligned with the collision axis, $\cos(\theta) = 1$, and (2) a maximum value for the C_{60} fullerane dipole moment, $\mu = (15)^{1/2}$ D (see Figure 7). For a collision energy corresponding to $T_K = 10$ K, the effective ion–dipole interaction distance is 8.0×10^{-7} cm, resulting in a collision cross section of $2.0 \times 10^{-12}\,cm^2$. The average geometric cross section for the above MRN distribution is $3.5 \times 10^{-12}\,cm^2$. Accounting for the 50% abundance of negatively charged grains, the ion–dipole interaction increases the accretion rate by, at most, a factor of 29% (i.e., 1/3.5). Given the uncertain and likely much smaller contribution of charged grains to the accretion rate, we did not include this effect in our estimate of the accretion timescale.

ORCID iDs

L. S. Bernstein https://orcid.org/0000-0001-6150-1579
R. M. Shroll https://orcid.org/0000-0002-7865-6769
C. Dickinson https://orcid.org/0000-0002-0045-442X

References

Adjizian, J.-J., Vlandas, A., Rio, J., Charlier, J.-C., & Ewels, C. P. 2016, RSPTA, 374, 20150323
Agúndez, M., Roueff, E., Le Petit, F., & Le Bourlot, J. 2018, A&A, 616, A19
Ali-Haïmoud, Y. 2014, MNRAS, 437, 2728
Ali-Haïmoud, Y., Hirata, C. M., & Dickinson, C. D. 2009, MNRAS, 395, 1055

Ali-Haïmoud, Y., Pérez, L. M., Maddalena, R. J., & Roshi, D. A. 2014, MNRAS, 447, 315
Allain, T., Leach, S., & Sedlmayr, E. 1996, A&A, 305, 602
AMI Consortium 2009, MNRAS, 396, 365
AMI Consortium, Scaife, A. M., Nikolic, B., et al. 2010, MNRAS, 406, L45
Andrews, H., Boersma, C., Werner, M. W., et al. 2015, ApJ, 807, 99
Battistelli, E. S., Carretti, E., Cruciani, A., et al. 2015, ApJ, 801, 111
Berkowitz, J. 1999, JChPh, 111, 1446
Berné, O., Cox, N. L. J., Mulas, G., & Joblin, C. 2017, A&A, 605, L1
Berné, O., Montillaud, J., & Joblin, C. 2015, A&A, 577, A133
Berné, O., Mulas, G., & Joblin, C. 2013, A&A, 550, L4
Berné, O., & Tielens, A. G. G. M. 2012, PNAS, 109, 401
Bernstein, L. S., Clark, F. O., Cline, J. A., & Lynch, D. K. 2015, ApJ, 813, 122
Bernstein, L. S., Shroll, R. M., Galazutdinov, G. A., & Beletsky, Y. 2018, ApJ, 859, 174
Bernstein, L. S., Shroll, R. M., Lynch, D. K., & Clark, F. O. 2017, ApJ, 836, 229
Bonaldi, A., Ricciardi, S., Leach, S., et al. 2007, MNRAS, 382, 1791
Bot, C., Ysard, N., Paradis, D., et al. 2010, A&A, 523, A20
Byrd, R. H., Lu, P., Nocedal, J., & Zhu, C. 1995, SIAM Journal on Scientific Computing, 16, 1190
Cami, J., Bernard-Salas, J., Peeters, E., & Malek, S. E. 2010, Sci, 329, 1180
Cami, J., Bernard-Salas, J., Peeters, E., & Malek, S. E. 2011, in Proc. IAU 7, 216
Cami, J., & Cox, N. L. J. 2014, in IAU Symp. 297, The Diffuse Interstellar Bands (Cambridge: Cambridge Univ. Press)
Cami, J., Peeters, E., Bernard-Salas, J., Doppmann, G., & De Buizer, J. 2018, Galax, 6, 101
Campbell, E. K., Holz, M., Gerlich, D., & Maier, J. P. 2015, Natur, 523, 322
Candian, A., Bouwman, J., Hemberger, P., Bodi, A., & Tielens, A. G. G. M. 2018a, Phys. Chem. Chem. Phys., 20, 5399
Candian, A., Tielens, A. G. G. M., & Zhen, J. 2018b, PhT, 71, 38
Cardillo, M., Tavani, M., Giuliani, A., et al. 2014, A&A, 565, A74
Casassus, S., Cabrera, G. F., Förster, F., et al. 2006, ApJ, 639, 951
Casassus, S., Dickinson, C., Cleary, K., et al. 2008, MNRAS, 391, 1075
Castellanos, P., Berné, O., Sheffer, Y., Wolfire, M. G., & Tielens, A. G. G. M. 2014, ApJ, 794, 8
Chai, J.-D., & Head-Gordon, M. 2008, Phys. Chem. Chem. Phys., 10, 661
Cox, N. L., Cami, J., Farhang, A., et al. 2017, A&A, 606, A76
Dickinson, C., Ali-Haïmoud, Y., Barr, A., et al. 2018, NewAR, 80, 1
Draine, B. T. 1978, ApJS, 36, 595
Draine, B. T. 2004, Astrophysics of Dust in Cold Clouds. In The Cold Universe (Berlin: Springer), 213
Draine, B. T., & Hensley, B. S. 2012, ApJ, 757, 103
Draine, B. T., & Hensley, B. S. 2016, ApJ, 831, 59
Draine, B. T., & Lazarian, A. 1998a, ApJ, 508, 157
Draine, B. T., & Lazarian, A. 1998b, ApJL, 494, L19
Draine, B. T., & Li, A. 2007, ApJ, 657, 810
Ehrenfreund, P., & Foing, B. H. 2010, Sci, 329, 1159
Finkbeiner, D. P. 2004, ApJ, 614, 186
Finkbeiner, D. P., Schlegel, D. J., Frank, C., & Heiles, C. 2002, ApJ, 566, 898
Frisch, M. J., Trucks, G. W., Schlegel, H. B., et al. 2009, Gaussian03, Revision E.01 (Wallingford, CT: Gaussian, Inc.), Gaussian 03, Revision E.01
Galazutdinov, G. A., Curto, G. L., & Krełowski, J. 2008, MNRAS, 386, 2003
García-Hernández, D. A., Manchado, A., García-Lario, P., et al. 2010, ApJ, 724, L39
Génova-Santos, R., Martín, J. R., Rebolo, R., et al. 2015, MNRAS, 452, 4169
Génova-Santos, R., Rubiño-Martín, J. A., Peláez-Santos, A., et al. 2016, MNRAS, 464, 4107
Głuch, K., Matt-Leubner, S., Echt, O., et al. 2004, JChPh, 121, 2137
Greaves, J. S., Scaife, A. M. M., Frayer, D. T., et al. 2018, NatAs, 2, 662
Hariharan, P. C., & Pople, J. A. 1985, AcTC, 28, 213
Harper, S. E., Dickinson, C., & Cleary, K. 2015, MNRAS, 453, 3375
Hay, P. J., & Wadt, W. R. 1985, JChPh, 82, 270
Hehre, W. J., Ditchfield, R., & Pople, J. A. 1972, JChPh, 56, 2257
Hensley, B. S., & Draine, B. T. 2017, ApJ, 836, 179
Hensley, B. S., Draine, B. T., & Meisner, A. M. 2016, ApJ, 827, 45
Herbig, G. H. 1995, ARA&A, 33, 19
Herbst, E. 2017, IRPC, 36, 287
Heyer, M., & Dame, T. M. 2015, ARA&A, 53, 583
Hoang, T., Draine, B. T., & Lazarian, A. 2010, ApJ, 715, 462
Hoang, T., Vinh, N. A., & Lan, N. Q. 2016, ApJ, 824, 18
Iglesias-Groth, S. 2005, ApJL, 632, L25
Iglesias-Groth, S. 2006, MNRAS, 368, 1925
Iglesias-Groth, S. 2011, MNRAS, 411, 1857
Irfan, M. O., Dickinson, C., Davies, R. D., et al. 2015, MNRAS, 448, 3572
Israel, F. P., Wall, W. F., Raban, D., et al. 2010, A&A, 519, A67
Jeloaica, L., & Sidis, V. 1999, CPL, 300, 157
Jensen, P. A., Leccese, M., Simonsen, F. D., et al. 2019, MNRAS, 486, 5492
Joblin, C., Berné, O., Simon, A., & Mulas, G. 2009, in ASP Conf. Ser. 44, 383
Jones, A. P. 2016, RSOS, 3, 160223
Jones, A. P., Tielens, A. G. G. M., & Hollenbac, D. J. 1996, ApJ, 469, 740
Kietzmann, H., Rochow, R., & Ganteför, G. 1998, PhRvL, 81, 5378
Kogut, A., Banday, A. J., Bennett, C. L., et al. 1996, ApJ, 464, L5
Koponen, L., Puska, M. J., & Nieminen, R.M. 2008, JChPh, 128, 154307
Krasheninnikov, A. V., & Nordlund, K. 2010, JAP, 107, 3
Kroto, H. 1988, Sci, 242, 1139
Kroto, H. W. 1987, Natur, 329, 529
Leach, S. M., Cardoso, J. F., Baccigalupi, C., et al. 2008, A&A, 491, 597
Leitch, E. M., Readhead, A. C. S., Pearson, T. J., & Myers, S. T. 1997, ApJ, 486, L23
Li, A., & Draine, B. T. 2001, ApJ, 554, 778
Loru, S., Pellizzoni, A., Egron, E., et al. 2018, MNRAS, 482, 3857
Luong, Q. N., Motte, F., Schuller, F., et al. 2011, A&A, 529, A41
Mackie, C. J., Chen, T., Candian, A., Lee, T. J., & Tielens, A. G. G. M. 2018, JChPh, 149, 134302
Małolepsza, E., Witek, H. A., & Irle, S. J. 2007, Phys. Chem. A, 111, 6649
Mathis, J. S., Rumpl, W., & Nordsieck, K. H. 1977, ApJ, 217, 425
Meny, C., Gromov, V., Boudet, N., et al. 2007, A&A, 468, 171
Micelotta, E. R., Jones, A. P., & Tielens, A. G. G. M. 2011, A&A, 526, A52
Minenkov, Y., Singstad, A., Occhipinti, G., & Jensen, V. R. 2012, Dalton Trans., 41, 5526
Montillaud, J., & Joblin, C. 2014, A&A, 567, A45
Montillaud, J., Joblin, C., & Toublanc, D. 2013, A&A, 552, A15
Mulliken, R. S. 1955, JChPh, 23, 1833
Murphy, E., Helou, G., Condon, J. J., et al. 2010, ApJL, 709, L108
Murphy, E. J., Linden, S. T., Dong, D., et al. 2018, ApJ, 862, 20
Oka, T., Welty, D. E., Johnson, S., et al. 2013, ApJ, 773, 42
Omont, A. 2016, A&A, 590, A52
Pagani, L., Roueff, E., & Lesaffre, P. 2011, ApJL, 739, L35
Peeters, E. 2011, in Proc. IAU 7, The PAH Hypothesis After 25 years, 149
Pilleri, P., Montillaud, J., Berné, O., & Joblin, C. 2012, A&A, 542, A69
Planck Collaboration 2011a, A&A, 536, A17
Planck Collaboration 2011b, A&A, 536, A20
Planck Collaboration 2013, A&A, 557, A53
Planck Collaboration 2014, A&A, 565, A103
Rapacioli, M., Joblin, C., & Boissel, P. 2005, A&A, 429, 193
Rathborne, J. M., Lada, C. J., Muench, A. A., et al. 2009, ApJ, 699, 742
Rauls, E., & Hornekær, L. 2008, ApJ, 679, 531
Remy, Q., Grenier, I. A., Marshall, D. J., & Casandjian, J. M. 2017, A&A, 601, A78
Roberts, K. R. G., Smith, K. T., & Sarre, P. J. 2012, MNRAS, 421, 3277
Rothe, E. W., & Bernstein, R. B. 1959, JChPh, 31, 1619
Scaife, A. M. M. 2013, AdAst, 2013, 390287
Schmidt, M. W., Baldridge, K. K., Boatz, J. A., et al. 1993, JCoCh, 14, 1347
Sellgren, K., Werner, M. W., Ingalls, J. G., et al. 2010, ApJ, 722, L54
Silsbee, K., Ali-Haïmoud, Y., & Hirata, C. M. 2011, MNRAS, 411, 2750
Snow, T. P., & McCall, B. J. 2006, ARA&A, 44, 67
Snow, T. P., & Witt, A. N. 1995, Sci, 270, 1455
Sun, D. Y., Liu, J. W., Gong, X. G., & Liu, Z. F. 2007, PhRvB, 75, 075424
Tibbs, C. T., Paladini, R., Cleary, K., et al. 2015a, MNRAS, 453, 3356
Tibbs, C. T., Paladini, R., Cleary, K., et al. 2015b, MNRAS, 456, 2290
Tielens, A. G. G. M. 2008, ARA&A, 46, 289
Ulbricht, H., Moos, G., & Hertel, T. 2003, PhRvL, 90, 095501
Virtanen, P., Gommers, R., & Oliphant, T.E. 2020, Nature Methods, 17, 261
Walker, G. A., Webster, A. S., Bohlender, D. A., & Krełowski, J. 2001, ApJ, 561, 272
Walker, G. A. H., Bohlender, D. A., Maier, J. P., & Campbell, E. K. 2015, ApJL, 812, L8
Watson, R. A., Rebolo, R., Rubiño-Martín, J. A., et al. 2005, ApJL, 624, L89
Webster, A. 1996, MNRAS, 282, 1372
Weingartner, J. C., & Draine, B. T. 1999, ApJ, 517, 292
Weingartner, J. C., & Draine, B. T. 2001a, ApJ, 548, 296
Weingartner, J. C., & Draine, B. T. 2001b, ApJS, 134, 263
Williams, J. P., & Cieza, L. A. 2011, ARA&A, 49, 67
Xie, Y., Ho, L. C., Li, A., & Shangguan, J. 2018, ApJ, 867, 91
Ysard, N., & Verstraete, L. 2010, A&A, 509, A12
Zhang, Y., Sadjadi, S., Hsia, C. H., & Kwok, S. 2017, ApJ, 845, 76
Zhu, C., Byrd, R. H., Lu, P., & Nocedal, J. 1997, ACM Transactions on Mathematical Software, 23, 550